Article

Cell Reports

A joint-ParB interface promotes Smc DNA recruitment

Graphical abstract

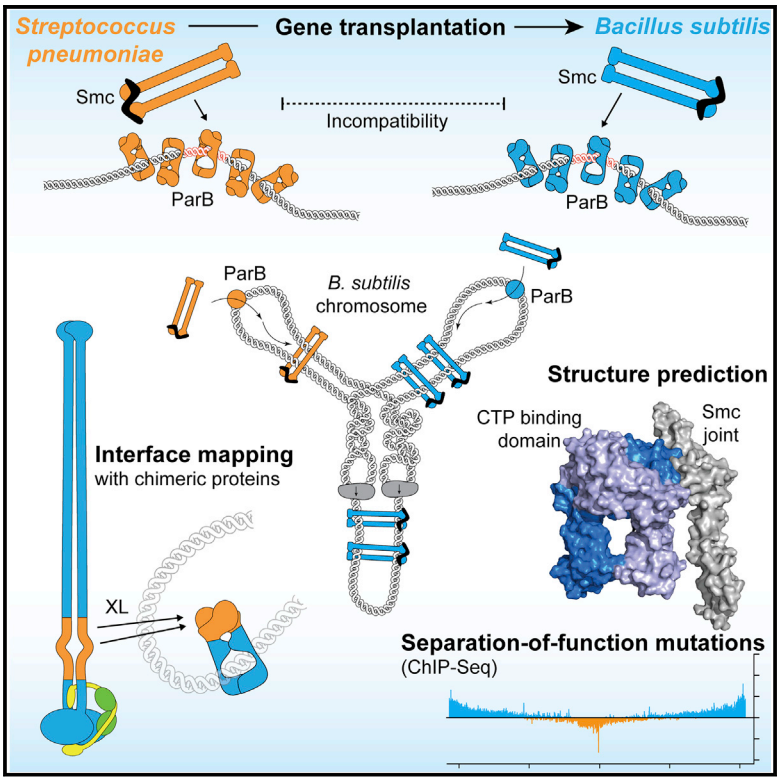

Highlights

- The bacterial DNA-binding protein ParB interacts with the condensin-like Smc-ScpAB
- Genetic mapping and structure predictions reveal an Smc joint-ParB binding interface
- Mutating the binding interface hampers Smc recruitment but not other ParB functions
- ParB and Smc-ScpAB form a transplantable unit for chromosome segregation in bacteria

Authors

Florian P. Bock, Hon Wing Liu, Anna Anchimiuk, Marie-Laure Diebold-Durand, Stephan Gruber

Correspondence

stephan.gruber@unil.ch

In brief

By transplanting *Streptococcus* genes into *Bacillus subtilis*, Bock et al. demonstrate that a four-gene module comprising genes encoding ParB and the condensin-like subunits Smc, ScpA, and ScpB can promote chromosome segregation in foreign bacteria. They elucidate a ParB-Smc protein-protein interface and show it is required for Smc recruitment by ParB.

Bock et al., 2022, Cell Reports *40*, 111273
August 30, 2022
https://doi.org/10.1016/j.celrep.2022.111273

CellPress

Cell Reports

CellPress
OPEN ACCESS

Article

A joint-ParB interface promotes Smc DNA recruitment

Florian P. Bock,[1] Hon Wing Liu,[1] Anna Anchimiuk,[1] Marie-Laure Diebold-Durand,[1] and Stephan Gruber[1,2,*]
[1]Department of Fundamental Microbiology (DMF), Faculty of Biology and Medicine (FBM), University of Lausanne, 1015 Lausanne, Switzerland
[2]Lead contact
*Correspondence: stephan.gruber@unil.ch
https://doi.org/10.1016/j.celrep.2022.111273

SUMMARY

Chromosomes readily unlink and segregate to daughter cells during cell division, highlighting a remarkable ability of cells to organize long DNA molecules. SMC complexes promote DNA organization by loop extrusion. In most bacteria, chromosome folding initiates at dedicated start sites marked by the ParB/*parS* partition complexes. Whether SMC complexes recognize a specific DNA structure in the partition complex or a protein component is unclear. By replacing genes in *Bacillus subtilis* with orthologous sequences from *Streptococcus pneumoniae*, we show that the three subunits of the bacterial Smc complex together with the ParB protein form a functional module that can organize and segregate foreign chromosomes. Using chimeric proteins and chemical cross-linking, we find that ParB directly binds the Smc subunit. We map an interface to the Smc joint and the ParB CTP-binding domain. Structure prediction indicates how the ParB clamp presents DNA to the Smc complex, presumably to initiate DNA loop extrusion.

INTRODUCTION

Organizing DNA for chromosome segregation is a fundamental challenge in biology. Structural maintenance of chromosomes (SMC) complexes fold DNA into a loop or multiple loops by a process called DNA loop extrusion (Yatskevich et al., 2019). They are found in all domains of life. Three types of SMC complexes with dedicated functions (i.e., Smc5/6, cohesin, and condensin) are nearly ubiquitous in eukaryotes (Yoshinaga and Inagaki, 2021). In prokaryotes, the Smc-ScpAB complex is predominant—being widely distributed in bacteria and present in some archaea. Disruption of any of the three subunits of Smc-ScpAB results in defective chromosome segregation in *Bacillus subtilis*, ultimately leading to cell death when grown on nutrient-rich medium that promotes fast DNA replication (Gruber et al., 2014). Other bacterial SMC variants, MukBEF and MksBEF(G), are highly diverged, with the latter supporting plasmid restriction rather than chromosome segregation in some bacteria (Panas et al., 2014; Petrushenko et al., 2011).

The Smc-ScpAB complex is recruited to the replication origin region of the bacterial chromosome by 16 base pair (bp) palindromic "*parS*" DNA sequences that associate with ParB protein (Gruber and Errington, 2009; Sullivan et al., 2009). Smc-ScpAB then starts translocating onto *parS*-flanking DNA in both orientations (Figure 1A). This bidirectional DNA translocation (i.e., DNA loop extrusion) brings together loci distantly located on opposing chromosome arms (Tran et al., 2017; Wang et al., 2017), which is thought to help separate nascent sister chromosomes, presumably by removing DNA entanglements in the wake of the DNA replication forks (Bürmann and Gruber, 2015). How Smc-ScpAB recognizes the *parS* loading site, how it loads onto DNA, and how it starts loop extrusion is poorly understood.

ParABS systems promote the partitioning of bacterial chromosomes and the stable maintenance of low copy-number plasmids. They comprise the *parS* sites, the ParA ATPase, and the ParB CTPase. The ParB protein is locally enriched in a "partition complex" by binding the cofactor CTP and clamping onto *parS* DNA (Figure 1A). The clamps then spread onto flanking DNA by 1D diffusion and recruit further ParB dimers before eventually unloading from the chromosome upon CTP hydrolysis (Antar et al., 2021; Jalal et al., 2021; Osorio-Valeriano et al., 2021; Soh et al., 2019; Tisma et al., 2022). ParB comprises three globular domains (Figure 2B). The amino-terminal "N domain" harbors the CTP binding pocket. It homodimerizes upon contact with *parS* DNA, thus closing the ParB clamp. The middle "M domain" includes a helix-turn-helix motif that specifically recognizes *parS* DNA (Chen et al., 2015). The carboxy-terminal "C domain" serves to dimerize two ParB monomers and promotes sequence-nonspecific DNA binding (Fisher et al., 2017; Schumacher and Funnell, 2005). ParA forms gradients on the bacterial chromosome along which the partition complexes move to equiposition themselves (Hwang et al., 2013; Lim et al., 2014). This requires stimulation of ParA ATP hydrolysis by an N-terminal peptide on ParB, which converts DNA-bound ParA dimers into cytosolic monomers (Gruber and Errington, 2009; Scholefield et al., 2011; Zhang and Schumacher, 2017).

Smc proteins fold into a highly elongated particle having an ABC-type ATPase "head" domain at one end and a dimerization "hinge" domain at the other end of a long intramolecular antiparallel coiled-coil "arm" (Figure 1A) (Haering et al., 2002). The kleisin

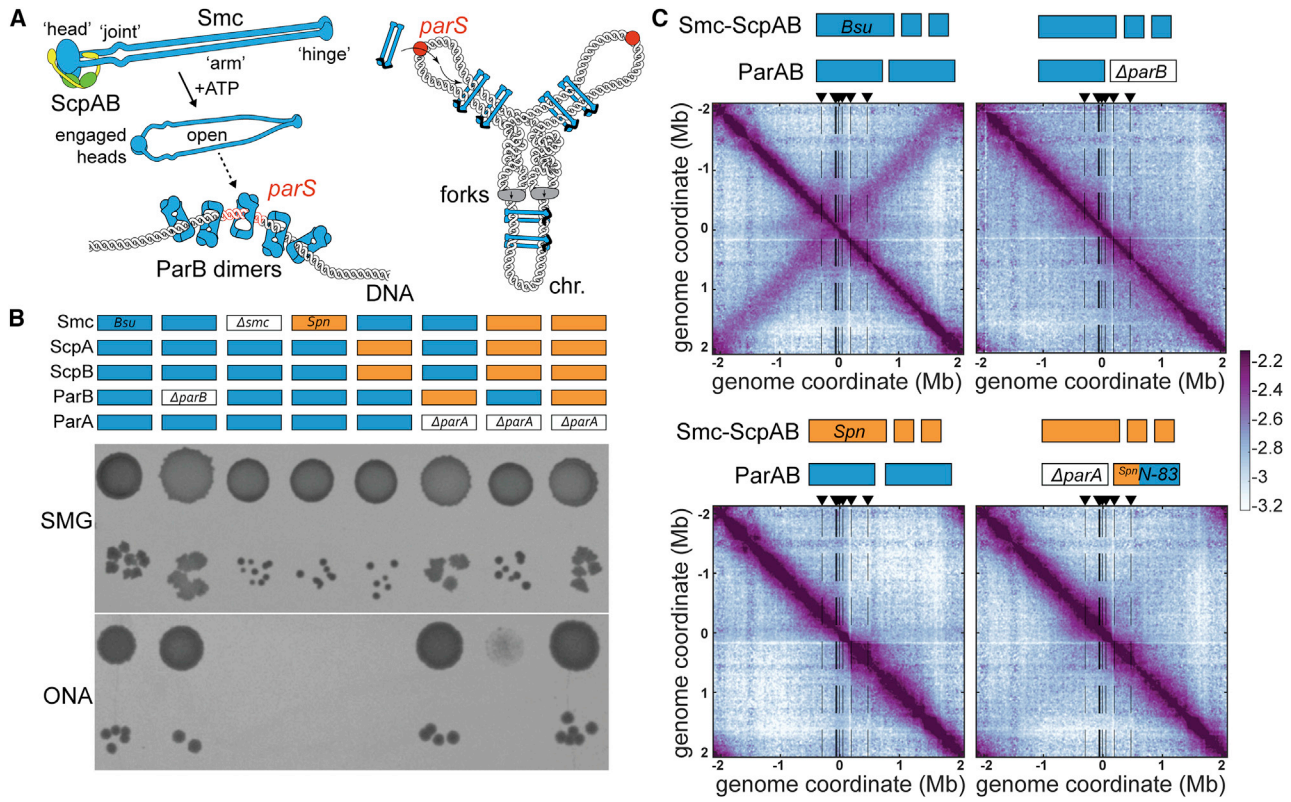

Figure 1. A four-component system for chromosome organization in bacteria

(A) Schematic of Smc recruitment via ParB at *parS* sites (left) and chromosome organization by DNA loop extrusion (right). Chromosome, chr.; DNA replication forks, forks.

(B) Viability assessment of gene-transplanted strains by spotting on nutrient-poor medium (SMG) and nutrient-rich medium (ONA). Gene identity of strains indicated by colored bars, *Bsu* in blue colors, *Spn* in orange colors. Spotting was performed in technical triplicates.

(C) Normalized 3C-seq contact maps of strains with the indicated genotypes from exponentially growing cultures. Additional maps are shown in Figure S1. All 3C-seq contact maps presented are divided into 10-kb bins with the replication origin being placed in the middle. The interaction score is on a log10 scale (for more details, see STAR Methods). Note that the contact map for the wild type is the same as in Anchimiuk et al. (2021). The 3C-seq experiments were performed in biological duplicates yielding comparable results. See also Figure S1.

protein ScpA connects the head domain of one Smc subunit to the head-proximal arm ("neck") of the other, together forming a ring-shaped protein complex capable of entrapping chromosomal DNA (Bürmann et al., 2013; Gligoris et al., 2014; Wilhelm et al., 2015). Two ScpB proteins—belonging to the kite family—bind to the central region of ScpA (Palecek and Gruber, 2015). The two long Smc arms co-align to form a rod-shaped particle with misaligned head domains. ATP engagement of the head domains in turn pulls the arms apart, thus creating a more open ring-shaped particle (Vazquez Nunez et al., 2021) (Figure 1A). An essential DNA binding interface is formed by ATP-engaged Smc head domains. How DNA is clamped at the Smc heads and how DNA binding and ATP hydrolysis promote loop extrusion is not well understood (Vazquez Nunez et al., 2019).

Recruitment of Smc-ScpAB by the partition complex relies on several factors. Smc heads have to bind ATP and engage with one another, while ATP hydrolysis by Smc appears dispensable (Minnen et al., 2016). The hydrolysis-defective mutant Smc(E1118Q) ("EQ") efficiently targets *parS* DNA, especially when Smc arm alignment is artificially weakened (e.g., by mutations preventing hinge dimerization). The accumulation of Smc(EQ) at *parS* DNA requires DNA clamping by ATP-engaged Smc heads (Vazquez Nunez et al., 2019). DNA clamping by ParB is essential for Smc recruitment, while CTP hydrolysis is dispensable (Antar et al., 2021). Altogether, this suggests that an open, ATP-bound, DNA-clamping state of Smc-ScpAB associates with the ParB DNA sliding clamp. The interface between Smc-ScpAB and ParB, however, has remained elusive, possibly owing to the weak and transient nature of the interaction or the dependence on so-far unknown cofactors. In addition, the relationship of DNA in the ParB clamp and the Smc clamp is unclear.

Here, we provide conclusive evidence that ParABS promotes chromosome folding via a direct protein-protein interaction between the ParB protein and the Smc-ScpAB complex. Using chimeric proteins and site-specific *in vivo* cross-linking, we identify the key residues for specifying the interaction. These residues are located on the Smc joint and the recently discovered CTP-controlled N-terminal DNA-gate domain of ParB (Antar et al., 2021; Soh et al., 2019). Structure prediction provides first insights into how the ParB clamp may feed DNA into the

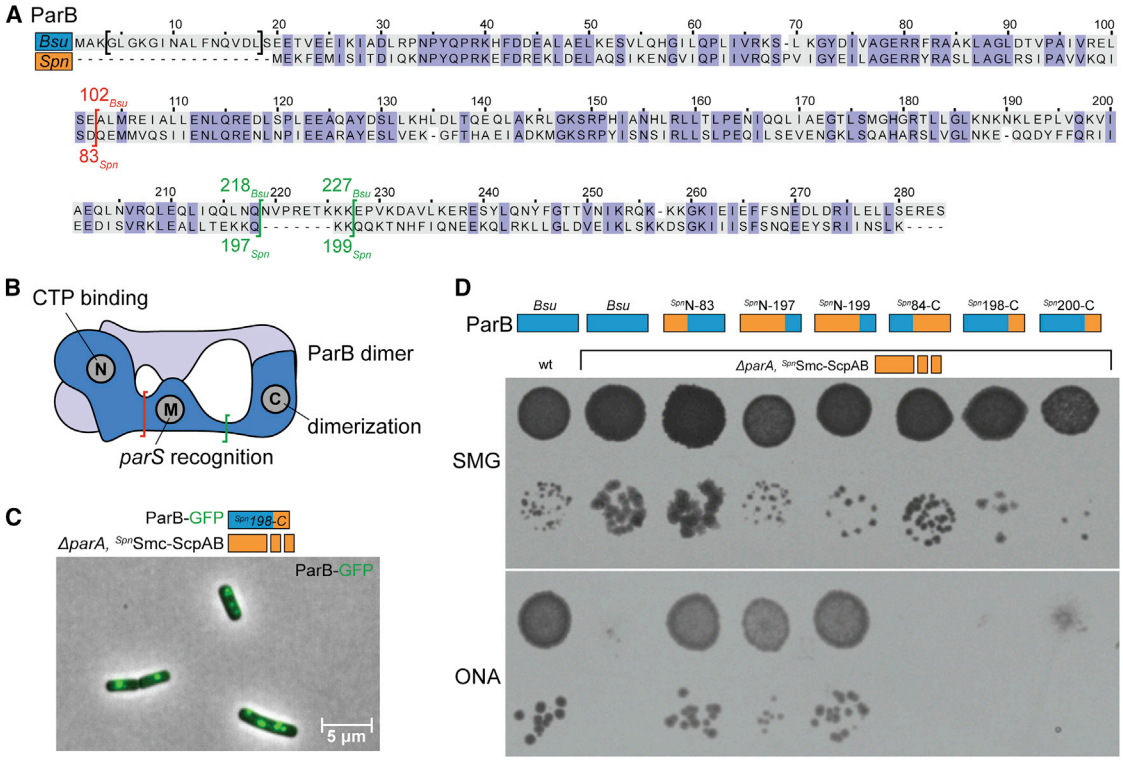

Figure 2. Smc binds the ParB N domain

(A) Alignment of *Bsu* and *Spn* ParB protein sequences. Identical residues are denoted by blue background colors, divergent residues in gray colors. Construction of ParB chimeras is indicated in red colors at the N to M domain transition and in green colors at the M to C domain transition. The black brackets denote ParA-interacting residues that were removed from chimeric constructs harboring N-terminal sequences of *Bsu* origin.

(B) ParB domain structure. Constructions of chimeras are indicated by brackets.

(C) Microscopy image of *B. subtilis* cells harboring ^{Spn}Smc-ScpAB with the ^{Spn}198-C ParB chimera fused to GFP protein. See Figure S2C for other chimeras.

(D) Spotting assay of *B. subtilis* strains carrying ^{Spn}Smc-ScpAB as well as the indicated chimeric ParB proteins, as in Figure 1B. Spotting was performed in technical triplicates. See also Figure S2.

Smc-ScpAB complex for loop extrusion. We further demonstrate that the Smc-ScpAB and ParB/*parS* complexes together form a minimal system for chromosome folding and segregation that can be transplanted from one bacterial species to another.

RESULTS

A four-gene module from *S. pneumoniae* promotes chromosome segregation in *B. subtilis*

To determine the minimal set of factors needed to organize and segregate chromosomes in bacteria, we replaced genes encoding components of the *B. subtilis* (*Bsu*) Smc holo-complex with orthologous counterparts. As gene donor, we chose *Streptococcus pneumoniae* (*Spn*), which also relies on Smc-ScpAB for efficient chromosome segregation (Minnen et al., 2011). The respective Smc genes display 38% amino acid sequence identity, implying that residues at the protein-protein interfaces have significantly coevolved. Substituting the *scpAB* operon, which encodes the ScpA and ScpB subunits, or the *smc* gene by the respective *Spn* orthologs, led to severe growth defects on nutrient-rich medium similar to the *Δsmc* mutant (Figure 1B). Combining the *smc* and *scpAB* genes of *Spn* origin only marginally improved growth on nutrient-rich medium, demonstrating that the genes encoding the subunits of the *Spn* Smc complex alone or in combination ("^{Spn}Smc-ScpAB") are unable to support chromosome segregation in *B. subtilis*. Chromosome folding was also altered in the ^{Spn}Smc-ScpAB strain, as judged from 3C-sequencing (3C-seq) contact maps (Figure 1C). Similar to the *ΔparB* mutant, contacts along the secondary diagonal originating from arm-arm co-alignment by Smc-ScpAB were missing (Figures 1C and S1) (Wang et al., 2017). Some ^{Bsu}Smc-ScpAB complexes load onto the chromosome in the absence of ParB protein, presumably at random positions, leading to residual contacts across the chromosome arms, which are widely distributed in the interarm quadrants (top-right and bottom-left) of the *ΔparB* contact map. In contrast, ^{Spn}Smc-ScpAB apparently fails to productively load onto the chromosome (despite the presence of ^{Bsu}ParB) as evident from a further reduction of interarm contacts. Residual loop extrusion activity by ^{Bsu}Smc-ScpAB may thus support chromosome segregation and cell viability in the *ΔparB* strain, while ^{Spn}Smc-ScpAB appears unable to support such an activity.

One explanation for the strong phenotypes associated with ^{Spn}Smc-ScpAB might be its inability to interact with host factors in *B. subtilis*, such as the ParB protein and *parS* sites. While the function of endogenous ^{Bsu}Smc-ScpAB does not strictly require

ParB or *parS*, ^{Spn}Smc-ScpAB may rely on (cognate) ParB even for basal functions. To test this possibility, we next substituted the *parB* gene. Since *S. pneumoniae* does not encode for ParA, we also deleted the *Bsu parA* gene to eliminate any detrimental effect of unregulated ParA (Murray and Errington, 2008; Quisel and Grossman, 2000). Moreover, we added a *parS* site at the 3′ end of the gene (Figure S2A), because *parB* naturally harbors an internal *parS* sequence in *B. subtilis* (Minnen et al., 2011). As expected from the mild phenotypes of Δ*parB* and Δ*parA* mutants, these modifications on their own did not noticeably alter growth (but caused a change in colony morphology) (Figure 1B). Introducing ^{Spn}ParB into strains already harboring ^{Spn}Smc and ^{Spn}ScpAB resulted in much-improved growth on nutrient-rich medium, with viability and growth comparable to those of wild-type cells (Figure 1B). Likewise, 3C-seq analysis showed increased levels of contacts across the left and right chromosome arms (when relevant parts of ParB comprised the *Spn* sequence; see below) (Figure 1C). The levels of these contacts were still reduced when compared with wild type, and their distribution was broadened, implying that ^{Spn}Smc-ScpAB is less efficient or less organized in forming these contacts (with all *parS* sites or only two *parS* sites present) (Figure S1) (Anchimiuk et al., 2021). Nevertheless, these results demonstrate that ^{Spn}Smc-ScpAB is principally capable of organizing the chromosome for efficient segregation in *B. subtilis*, but only when it is targeted to the replication origin region by the cognate ^{Spn}ParB.

Functional interactions of four proteins (ParB, Smc, ScpA, and ScpB) are thus needed for proper chromosome folding. Sequence divergence apparently prevents productive protein-protein interactions across the two species, rendering the *Bsu* and *Spn* modules orthogonal to one another. The critical involvement of additional proteins in chromosome folding by Smc is highly unlikely, as such factors would have to fruitfully interact with *Bsu* and *Spn* proteins despite their inability to function together.

Mapping ParB sequences promoting smc function

We next made use of the orthogonality of the chromosome folding modules to map protein binding interfaces between ParB and Smc-ScpAB. We engineered chimeric ParB proteins having either amino- or carboxy-terminal *Bsu* parts exchanged for the corresponding *Spn* sequences (Figure 2A). The sequence junctions were chosen at domain boundaries in regions of low sequence conservation to minimize protein folding problems (Figure 2B). Since *Spn* ParB lacks the N-terminal extension that normally stimulates ATP hydrolysis by ParA (Gruber and Errington, 2009; Leonard et al., 2005), we excluded these residues from any chimeric ParB sequences and also deleted *parA*. As expected, none of the chimeric ParB proteins led to obvious growth phenotypes in otherwise wild-type strains (Figure S2B). When introduced into an ^{Spn}Smc-ScpAB strain, all chimeric ParB proteins with amino-terminal domains of *Spn* origin (^{Spn}N-83, ^{Spn}N-197, and ^{Spn}N-199) promoted robust growth on nutrient-rich medium (Figure 2D). When instead the ParB carboxy-terminus originated from *S. pneumoniae* (^{Spn}84-C, ^{Spn}198-C, and ^{Spn}200-C), the strains showed poor growth on nutrient-rich medium as with full-length ^{Bsu}ParB (Figure 2D). As control, we fused the chimeric ParB proteins to GFP. Several fusion proteins showed clear focal localization but with variable fluorescence intensity (Figures 2C and S2C), presumably due to considerable variations in the expression levels as also observed by immunoblotting using anti-GFP serum (Figure S2D). ^{Spn}N-83-GFP and ^{Spn}N-197-GFP were particularly well expressed, while ^{Spn}84-C-GFP and ^{Spn}198-C-GFP were poorly expressed. Further mapping experiments (discussed below), however, suggest that differences in expression are unlikely to explain the above observations. The results rather indicate that the CTP-binding domain of ParB mediates a direct physical and functional interaction with Smc-ScpAB. 3C-seq analysis is consistent with this notion, as ^{Spn}Smc-ScpAB produced an increase in interarm chromosome contacts when ^{Bsu}ParB was substituted for ^{Spn}N-83 (Figure 1C).

Identifying residues in the CTP-binding domain of ParB critical for Smc association

We next set out to fine-map the Smc-binding interface on ParB by identifying ^{Spn}ParB residues that are required to support the activity of ^{Spn}Smc-ScpAB in *B. subtilis*. There are 38 residue differences in the N domain across ^{Bsu}ParB and ^{Spn}ParB. We focused on surface-exposed residues and grouped them into four patches for mutagenesis (denoted as patch 1 to 4) (Figure 3A). Exchange of all four patches in ^{Bsu}ParB for the corresponding *Spn* residues led to robust growth of the ^{Spn}Smc-ScpAB strain (Figure 3B) comparable to full exchange of the amino-terminal sequence (^{Spn}N-83), indicating that residues outside the chosen patches (8 in total) are not critically relevant. Strains harboring *Spn* residues in only three of the four patches exhibited different growth behaviors: A strain retaining *Bsu* residues only in patch 1 or in patch 3 failed to grow on nutrient-rich medium, highlighting their importance for the ParB-Smc interaction (Figure 3B). A strain harboring *Bsu* residues in patch 2 showed good growth, while a strain with a *Bsu* patch 4 displayed an intermediate phenotype. Accordingly, residues from patches 1, 3, and 4 significantly contribute to the interaction with Smc.

Following the same strategy, we subdivided the sequence into smaller patches: 1A, 1B, 1C, 3A, 3B, 4A, and 4B (Figure 3A). Converting these patches individually to the *Spn* sequence demonstrated that residues in 1B, 3B, 4A, and 4B are largely dispensable for promoting Smc-ParB interactions. In contrast, residues in patches 1A, 1C, and 3A appear critical (Figure 3C), with the conversion of patch 3A having a particularly severe impact on growth. 1A, 1C, and 3A together comprise eight residue differences, which mapped closely together on the surface of the ParB-CDP crystal structure (PDB: 6SDK) (Soh et al., 2019), likely delineating a Smc-binding interface on ParB (Figure 3D). Of note, these ParB chimeras (with one exception) supported growth of an *smc-pk3* strain (Gruber and Errington, 2009), which is sensitized for ParB function by the hypomorphic *smc* allele (Figure S3B). Moreover, the cellular levels of these chimeric ParB proteins are roughly comparable as judged by immunoblotting, and any variations do not correlate with the observed growth phenotypes when combined with ^{Spn}Smc-ScpAB (Figure S3C). The identified patches of residues thus likely support ^{Bsu}Smc-ScpAB function by promoting ParB-Smc associations.

Smc sequences crucial for ParB targeting

We next set out to identify Smc sequences responsible for association with ParB. Previous research uncovered a minimal Smc

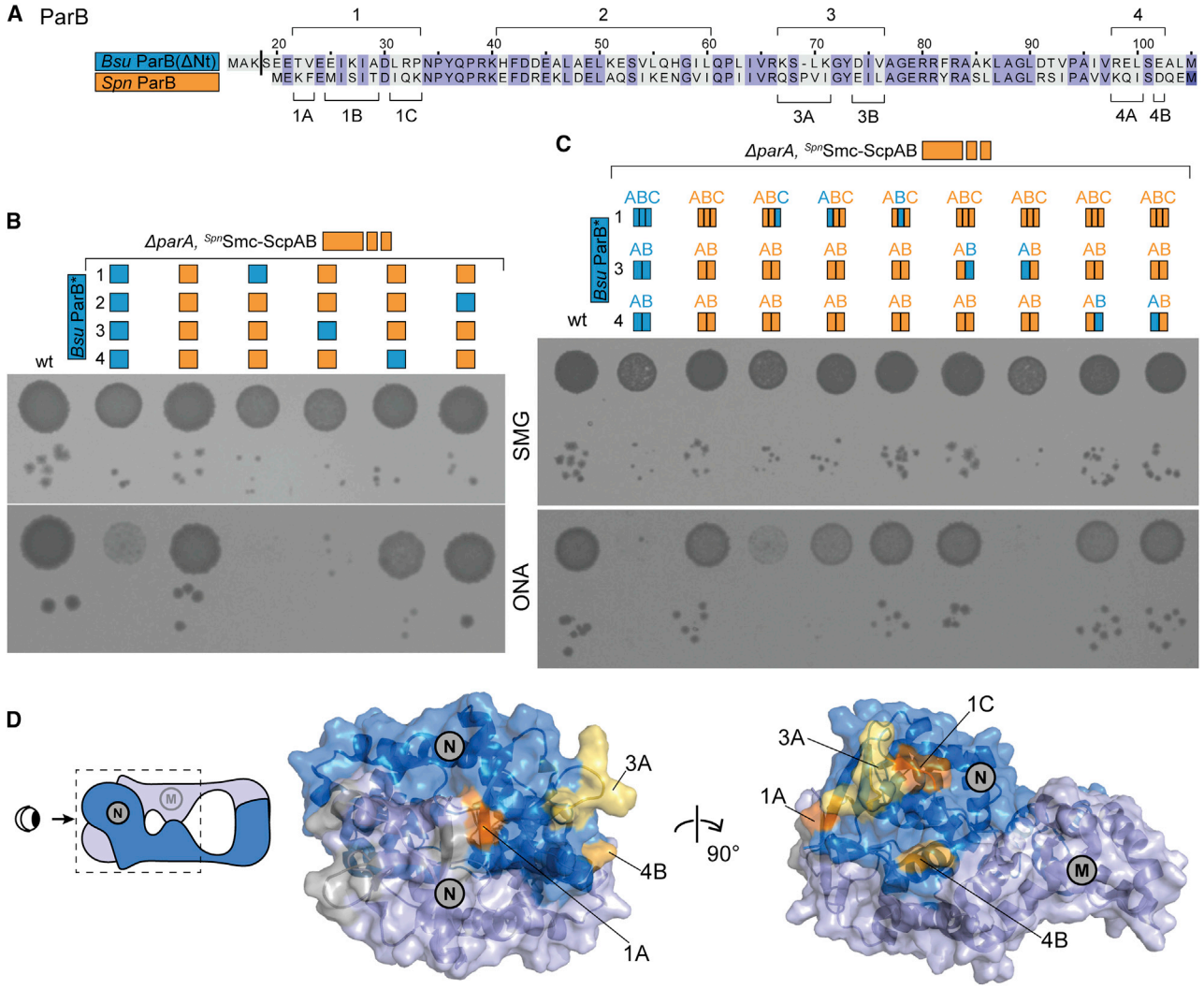

Figure 3. Fine mapping of the Smc-binding site on ParB

(A) Sequence alignment of *Bsu* and *Spn* ParB N domain, as in Figure 2A. Grouping of ParB residues in patches (1–4, top labels) as well as subgrouping (A, B, and C, bottom labels).

(B) Viability assay by dilution spotting for ^{Spn}Smc-ScpAB strains carrying chimeric ParB proteins, as defined in (A). As in Figure 1B. Spotting was performed in technical triplicates.

(C) As in (B) for additional ParB chimeras.

(D) Distribution of the identified Smc-interacting residues on the surface of the CTP-engaged ParB N-domain dimer (PDB: 6SDK [Soh et al., 2019]). ParB chains are shown in blue and gray colors, respectively. Key residues are indicated and highlighted in yellow, orange, and brown colors. Notably, the presence of *parA* significantly reduced the viability of some of the strains, indicating that ParA mis-regulation is not tolerated well by these ParB variants when also combined with ^{Spn}Smc-ScpAB (Figure S3A). See also Figure S3.

fragment that is proficient in *parS* targeting (Minnen et al., 2016). The fragment included the Smc head domain as well as approximately 70 amino acids of the head-proximal coiled-coil. *parS* targeting of this fragment required the Walker B motif mutation (E1118Q), which prevents ATP hydrolysis but supports ATP-head engagement. Whether the head domains directly promote ParB binding or are merely required for ATP-mediated dimerization of the Smc fragment or for ATP-dependent DNA binding, however, is unclear (Vazquez Nunez et al., 2019).

Building on available structural information and prior experience with chimeric Smc proteins (Bürmann et al., 2017; Diebold-Durand et al., 2017), we constructed Smc chimeras with head-proximal sequences of *Bsu* origin and hinge-proximal sequences of *Spn* origin (Figure 4A). Junctions were chosen within the Smc joint or in its proximity (ranging from Smc_{234} to Smc_{248}) with a crystal structure (PDB: 5NMO) helping to keep amino- and carboxy-terminal sequences in register (Figures 4A and S4A). All five chimeric proteins constructed in this fashion supported viability on nutrient-rich medium (Figure S4B), implying that they are well expressed and properly folded. Notably, this also implies that any physical interactions between distal parts of Smc (e.g., between the hinge and head domains upon putative elbow folding) are not critical.

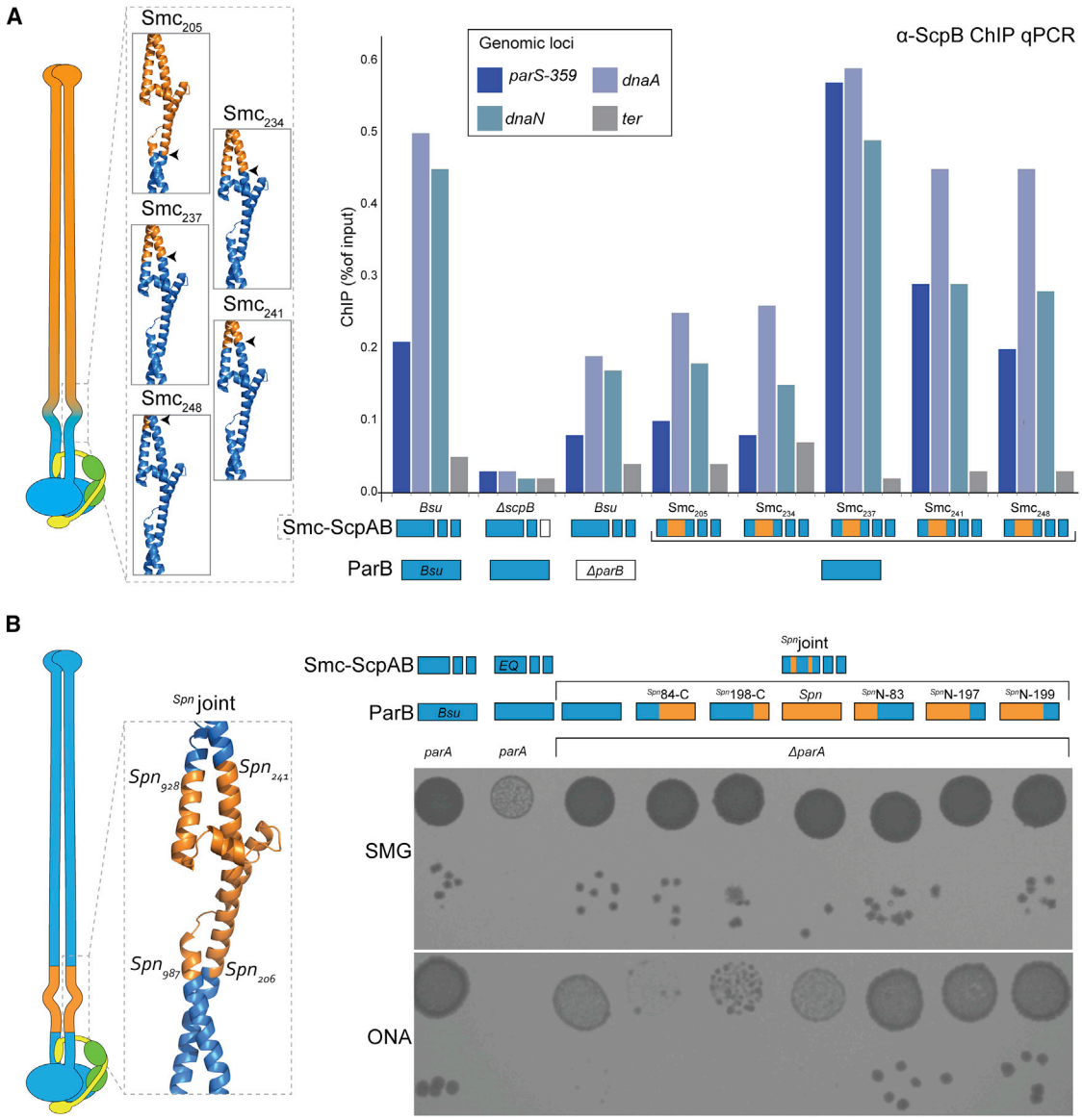

Figure 4. The Smc joint domain targets ParB

(A) Left: Schematic of Smc-ScpAB and the structure of the *Bsu* Smc joint (PDB: 5NMO) denoting the construction of chimeric Smc proteins, blue colors indicating *Bsu* sequence identity, orange colors indicating *Spn* origin. Right: Chromatin immunoprecipitation coupled to quantitative PCR (ChIP-qPCR) using α-ScpB serum undertaken with chimeric Smc strains as denoted. See additional experiments in Figure S4C.

(B) Left: Schematic and structural model of Smc protein; displayed as in (A). Right: Viability assay by spotting strains carrying ^{Spn}joint in combination with the indicated ParB chimeras. As in Figure 1B. Spotting was performed in technical triplicates. For the corresponding ChIP-qPCR results, see Figure S4D. See also Figure S4.

Given the robust functioning of these chimeric proteins in the presence of ^{Bsu}ParB, we assessed their targeting directly by performing chromatin immunoprecipitation with antiserum raised against the ScpB protein followed by quantitative PCR (ChIP-qPCR). This revealed three types of distribution patterns. Two chimeric proteins, Smc_{205} and Smc_{234}, displayed reduced targeting to origin-proximal sites, including the $parS_{359}$ site, as well as at the *dnaA* and *dnaN* genes, similar to the distribution found in a strain lacking *parB* (Figures 4A and S4C). These chimeric proteins thus appear to be unable to functionally interact with ^{Bsu}ParB. Two other chimeric proteins, Smc_{241} and Smc_{248}, showed normal or near-normal distributions. The fifth construct, Smc_{237}, displayed a phenotype of *parS*-hyperlocalization, possibly suggesting defective protein release from *parS* sites. Taken together, these results identify sequences in the Smc joint and the immediately adjacent coiled coil that mediate ParB-Smc interactions.

The Smc joint promotes ParB association

To test whether the Smc joint is sufficient to determine ParB specificity or whether head sequences are also necessary, we next constructed a chimeric Smc protein ("^{Spn}joint") having only joint sequences of *Spn* origin (Figure 4B). Replacement of

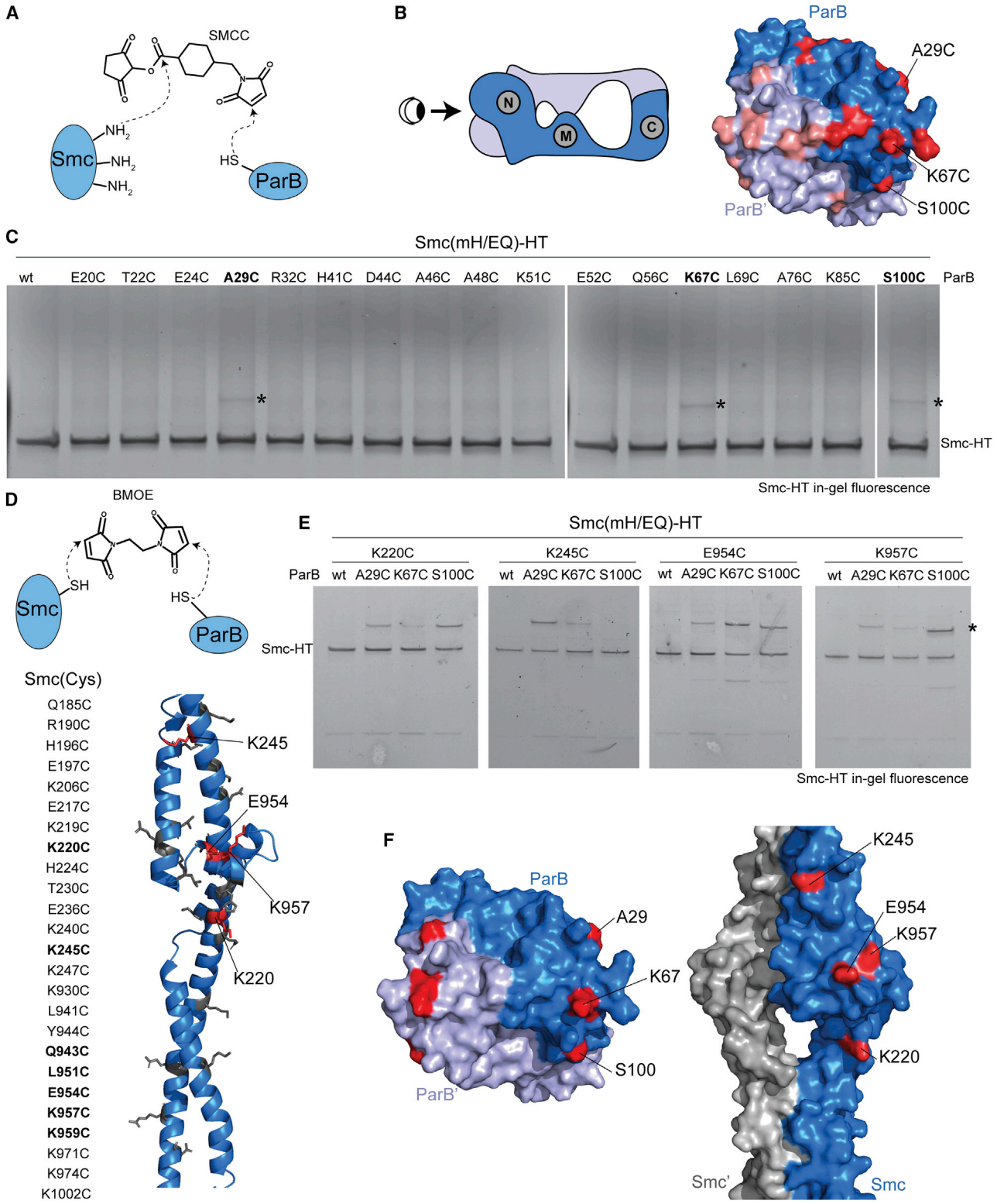

Figure 5. ***In vivo*** **cross-linking of ParB and Smc proteins.**

(A) Schematic of chemical cross-linking by the heterobifunctional molecule SMCC.

(B) Candidate ParB cysteine residues and their position (in red colors) on the ParB-CDP dimer (in surface representation with chains in blue and gray colors).

(C) SMCC cross-linking using ParB(Cys) mutants as indicated and detected by in-gel fluorescence detection of Smc(mH/EQ)-HT ("Smc-HT") protein. Higher molecular weight species appearing upon cross-linking are indicated by asterisks. Cross-linking was performed in technical duplicates.

(legend continued on next page)

^{Bsu}Smc against the ^{Spn}joint protein resulted in poor growth on nutrient-rich medium (Figure 4B), albeit noticeably better growth than *Δsmc*. The ^{Spn}joint protein is thus not fully functional, which can likely be ascribed to it being heavily engineered. Crucially, when combined with chimeric *parB* alleles having amino-terminal *Spn* sequences (^{Spn}N-83, ^{Spn}N-197, and ^{Spn}N-199), it supported robust growth, while the other *parB* alleles (^{Spn}84-C, ^{Spn}198-C, and ^{Spn}200-C) further decreased viability on nutrient-rich medium (Figure 4B). We found that these growth patterns correlated well with the chromosome distribution of ScpB in these strains, as determined by ChIP-qPCR analysis (Figure S4D). Of note, ^{Spn}ParB did not significantly improve the viability of the ^{Spn}joint strain or the recruitment of ^{Spn}Smc-ScpAB, possibly indicating that C-terminal ParB sequences might contact Smc-ScpAB sequences outside the Smc joint and thus contribute to Smc-ParB associations. Together, the above experiments show that sequences in the Smc joint and the ParB CTP-binding domain need to be matched to enable productive ParB-Smc interplay. This implies that a direct physical interaction between these regions is necessary for optimal function. The head domains likely contribute indirectly to the targeting of minimal Smc fragments by mediating Smc dimerization and DNA binding (Vazquez Nunez et al., 2019).

Proximity of ParB and Smc detected by chemical cross-linking

Next, we applied *in vivo* cross-linking to complement the mapping by genetics and to further fine-map the Smc-ParB interface. Given a lack of structural information on the interface at that time, we approached the problem in two steps. We first cross-linked candidate cysteine residues in ParB to lysine residues in Smc using the heterobifunctional Lys-Cys cross-linker SMCC (Figure 5A). In a second step, we used the homobifunctional Cys-Cys cross-linker BMOE (Figure 5D) on combinations of ParB(Cys) and Smc(Cys) mutants. To enhance the fraction of cellular Smc proteins localized at *parS* (Minnen et al., 2016), we used an EQ mutant also defective in hinge dimer formation ("mH") (Hirano and Hirano, 2002). The Smc protein also harbored a HaloTag ("HT") for quantitative detection of cross-linked species. Seventeen residues on the surface of ParB were selected to evenly cover the N-terminal sequence of ParB (Figure 5B). Only when ParB(A29C), ParB(K67C), and ParB(S100C) were used, we observed an additional, more slowly migrating species of Smc(mH/EQ)-HT (Figure 5C). We note that these three residues localize to patches 1, 3, and 4, respectively (Figure 3A). They are closely juxtaposed to each other on the surface of ParB (Figure 5B) and presumably located in proximity to one or more lysine residue(s) of Smc.

To identify the Smc residues that are in proximity to ParB, we selected 25 candidate residues located on both α-helices of the joint to be mutated to cysteines (Figure 5D). The mutations were generated in the Smc(mH/EQ)-HT protein and combined with the three ParB(Cys) mutants identified above. To improve the detection of cross-linked products, we enriched ParB species by pull-down assays with serum raised against the ParB protein. Comparable results were, moreover, obtained without prior enrichment (Figure S5B). We found relatively robust cross-linking with only four Smc(Cys) mutations: K220, K245, K954, and K957 (Figures 5E and S5B). These four residues were distributed in multiple α-helices of the Smc joint. However, all four were exposed on the same side of the Smc joint surface (Figure 5F).

Predicting the structure of the joint-ParB interface

We finally applied structure prediction using AlphaFold-Multimer (AF-Multimer) to the minimal interacting sequences identified by our mapping experiments (i.e., the Smc joint and ParB NM domains) (Evans et al., 2021). The folds of the two individual chains were predicted with high confidence, and the predictions superimposed well with published crystal structures of the Smc joint (PDB: 5NMO) and ParB NM domains (PDB: 6SDK). AF-Multimer consistently predicted a tightly fitted heterodimer of the two protein fragments (Figure 6A), albeit with a lower level of prediction confidence for the interface. Consistent with our mapping experiments, the "joint-ParB" interface is formed by the ParB N domain and the middle and head-distal regions of the Smc joint. The C_α-C_α distances measured for four efficiently cross-linked cysteine pairs (Figure S5B) (~8–17 Å) fit well in the range for BMOE cross-linking (Figure 6B) (Diebold-Durand et al., 2017). Moreover, ParB residues identified through the matching of sequences in chimeric proteins were found directly at the interface (Figure 6C). The AF-Multimer model thus likely closely resembles the ParB-Smc structure formed during the recruitment of Smc-ScpAB to the ParB partition complex.

To determine the physiological relevance of the predicted ParB-Smc contact, we generated point mutations in five ParB residues located at the putative interface (Figure 6D). We tested a quintuple and two triple mutants for their impact on ParB function, first in the sensitized background harboring the *smc-pk3* allele. The three mutants displayed variable degrees of growth retardation on nutrient-rich medium (Figure 6E). To reveal undesired Smc-independent effects of the mutations, we combined the *parB* mutants also with a *Δsmc* allele. The two triple mutants showed growth on minimal medium comparable to the *Δsmc* strain, while the quintuple mutant had a noticeable added growth defect (Figure 6E). One of the two triple mutants (*parB(L69S, K70E, E101K)*) was thus chosen for further analysis. The cellular levels of ParB(L69S, K70E, E101K) were similar to wild-type ParB as judged by immunoblotting (Figure 6F). An Smc-GFP fusion protein formed diffuse foci in *parB(L69S, K70E, E101K)*, indicating a reduced efficiency of Smc accumulation near the replication origin (Figure S6A). To measure the distribution of Smc-ScpAB on the chromosome, we performed ChIP followed by deep sequencing using antiserum raised against the ScpB

(D) Schematic of BMOE cross-linking chemistry (top) and candidate Smc(Cys) residues and their distribution on the Smc joint structure (cartoon representation).
(E) BMOE cross-linking using combinations of ParB(Cys) and Smc(Cys) mutants as indicated. Samples were enriched for ParB interacting material by incubation with α-ParB antibody coupled Dynabeads. Detection by in-gel fluorescence of Smc(mH/EQ)-HT ("Smc-HT") protein. Cross-linked ParB-Smc species are indicated by asterisks. Cross-linking was performed in technical duplicates.
(F) Positioning of identified cross-linking residues on ParB (left, as in [B]) and Smc (right, Smc joint in the rod configuration in surface representation). See also Figure S5.

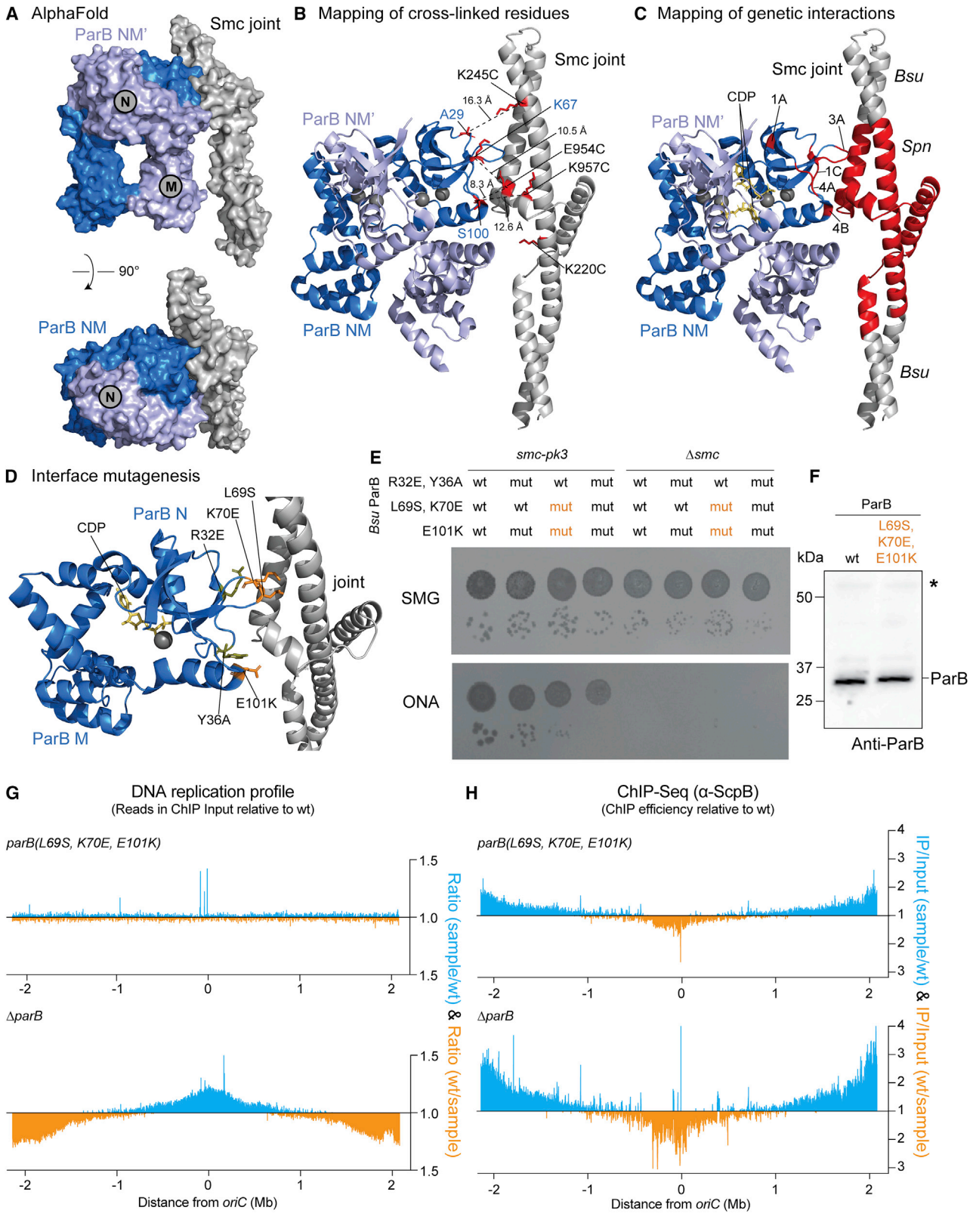

(legend on next page)

protein. As expected, the DNA profile of *ΔparB* input samples showed over-initiation of DNA replication, which is caused by uncontrolled ParA activity in the absence of ParB (Figures 6G and S6) (Murray and Errington, 2008). In contrast, the DNA profile of *parB(L69S, K70E, E101K)* was normal, indicating unperturbed ParABS functions in the control of DNA replication. Crucially, the ChIP read distributions in *parB(L69S, K70E, E101K)* exhibited reduced enrichment of the replication origin region and relative over-enrichment in original-distal regions of the chromosome when compared with wild-type cells (Figures 6H and S6), suggesting that the identified residues at the ParB-Smc interface indeed promote Smc recruitment. The defect is more pronounced in *ΔparB*, possibly due to residual recruitment of Smc by ParB(L69S, K70E, E101K) and/or by indirect effects caused by the mis-regulation of ParA protein in *ΔparB* (Murray and Errington, 2008). Altogether, these results identify ParB(L69S, K70E, E101K) as a long-sought separation-of-function mutant of ParB with compromised efficiency in Smc recruitment but normal ParA control. Of note, the intermediate growth phenotype explains why such *parB* mutants were not isolated in the screen for synthetic lethality in combination with *smc-pk3* (Gruber and Errington, 2009).

DISCUSSION

Revealing how SMC complexes load onto DNA is vital for a basic understanding of chromosome folding. Here, we provide insights into the delivery of DNA to an SMC complex by a bona fide loading factor (i.e., ParB), presumably to initiate DNA loop extrusion. We identified the joint-ParB interface as a major determinant for Smc targeting in bacteria.

Key functions of the SMC joint in DNA recruitment, loading, translocation, and unloading

SMC joints serve as a key recruitment platform in several SMC complexes. MatP and AcpP both associate with the MukB joint in MukBEF (Bürmann et al., 2021). MatP protein is an unloading factor for MukBEF, which releases it from the chromosome in the replication terminus region (Lioy et al., 2018). The AcpP protein has an important stimulatory effect on the ATPase activity of MukBEF (Prince et al., 2021). The hawk subunit Scc2 is a loading and processivity factor for DNA loop extrusion by cohesin (Davidson et al., 2019). It forms an interface with the Smc3 joint in the DNA-clamping state of cohesin (Higashi et al., 2020; Shi et al., 2020). An equivalent joint-hawk interface is also found in condensin (Lee et al., 2022; Shaltiel et al., 2022). The Smc3 joint (PDB: 6YUF) superimposes well with the bacterial Smc joint showing that the hawk-joint interface overlaps with the joint-ParB interface (Figure 7A) (Higashi et al., 2020). While ParB and hawk proteins are structurally and phylogenetically unrelated, they use equivalent binding sites on SMCs. The binding of cofactors to the joint, presumably to support DNA clamping, might thus be a general feature of many or all SMC complexes.

DNA loading by Smc-ScpAB

A key question for SMC-DNA loading is how chromosomal DNA first arrives at the DNA clamping site on top of ATP-engaged head domains (Vazquez Nunez et al., 2019). There are two possible scenarios (irrespective of SMC-kleisin-ring-DNA topology) (Figure 7B): A DNA double helix is transferred between disengaged heads and then becomes clamped on top of ATP-engaging Smc heads (scenario "1" in Figure 7B). Alternatively, heads first ATP-engage, thereby closing the route between the heads. A loop of DNA then engages directly from the coiled-coil proximal side (scenario "2" in Figure 7B) (Vazquez Nunez et al., 2019). Both scenarios are in principle compatible with the joint-ParB interface. We favor the second scenario, as it is easier to envision how ParB first contacts Smc and then promotes DNA engagement. The entry of DNA at the top of the heads has been suggested for DNA-end recognition by Rad50-Mre11 (Käshammer et al., 2019). At a DNA double-strand break, the DNA end can thread into the interarm space. In the case of Smc-ScpAB, however, a preformed DNA bend or loop has to thread into the interarm space. It is conceivable that such loops readily form in the ParB partition complex. In the case of phage P1, the DNA between *parS* site motifs is bent significantly by IHF protein binding (Surtees and Funnell, 2001). The details of such DNA passage, however, remain largely unclear.

The symmetric bacterial Smc dimer (Figure 7A) harbors two joint domains for ParB interaction. ParB may bind on the same

Figure 6. Prediction and evaluation of the joint-ParB interface structure

(A) Reconstruction of a Smc-ParB sub-complex by superimposition of the crystal structure of a ParB NM domain dimer (PDB: 6SDK) with a joint-ParB heterodimer predicted by AF-Multimer in surface representation in side view (top) and top view (bottom). The Smc chain is displayed in gray colors, and the ParB chains are displayed in dark and light blue colors, respectively.

(B) The Smc-ParB sub-complex shown in cartoon representation with residues used for cysteine cross-linking experiments highlighted as sticks in red colors. C_α-C_α distances (in Å) are indicated by dashed lines.

(C) Same as in (B) with Smc and ParB residues identified by genetic sequence matching displayed in red colors.

(D) Mutagenesis of selected residues (marked in stick representation) at the Smc-ParB interface. The predicted structure of the Smc joint (in gray colors) and the ParB NM domains (in marine colors) are displayed. The nucleotide CDP is shown in stick representation. Mutations that were pursued further are denoted in orange colors, other residues in olive colors.

(E) Viability assay by dilution spotting for candidate strains harboring Smc-binding interface mutants of ParB in *smc-pk3* and Δ*smc* backgrounds. Spotting was performed in technical triplicates.

(F) Immunoblotting to compare cellular levels of wild-type (WT) and mutant ParB using antiserum raised against *Bsu* ParB.

(G) Deep-sequencing DNA profiles of *parB(L69S,K70E,E101K)* and Δ*parB* input samples normalized to the DNA profile of WT cells. For bins with read counts greater than the WT sample, the ratio was plotted above the genome coordinate axis (in blue). Otherwise, the inverse ratio was plotted below the axis (in orange). Additional representations of the data are included in Figure S6.

(H) As in (G) but displaying ChIP efficiency (reads in IP/reads in Input) normalized to the ChIP efficiency obtained with WT cells. Ratios greater than 1 are displayed in blue, for other bins, the inverse ratio is shown in orange. ChIP-seq was performed on two biological replicates with comparable outcomes. Additional representations of the data are available in Figure S6. See also Figure S6.

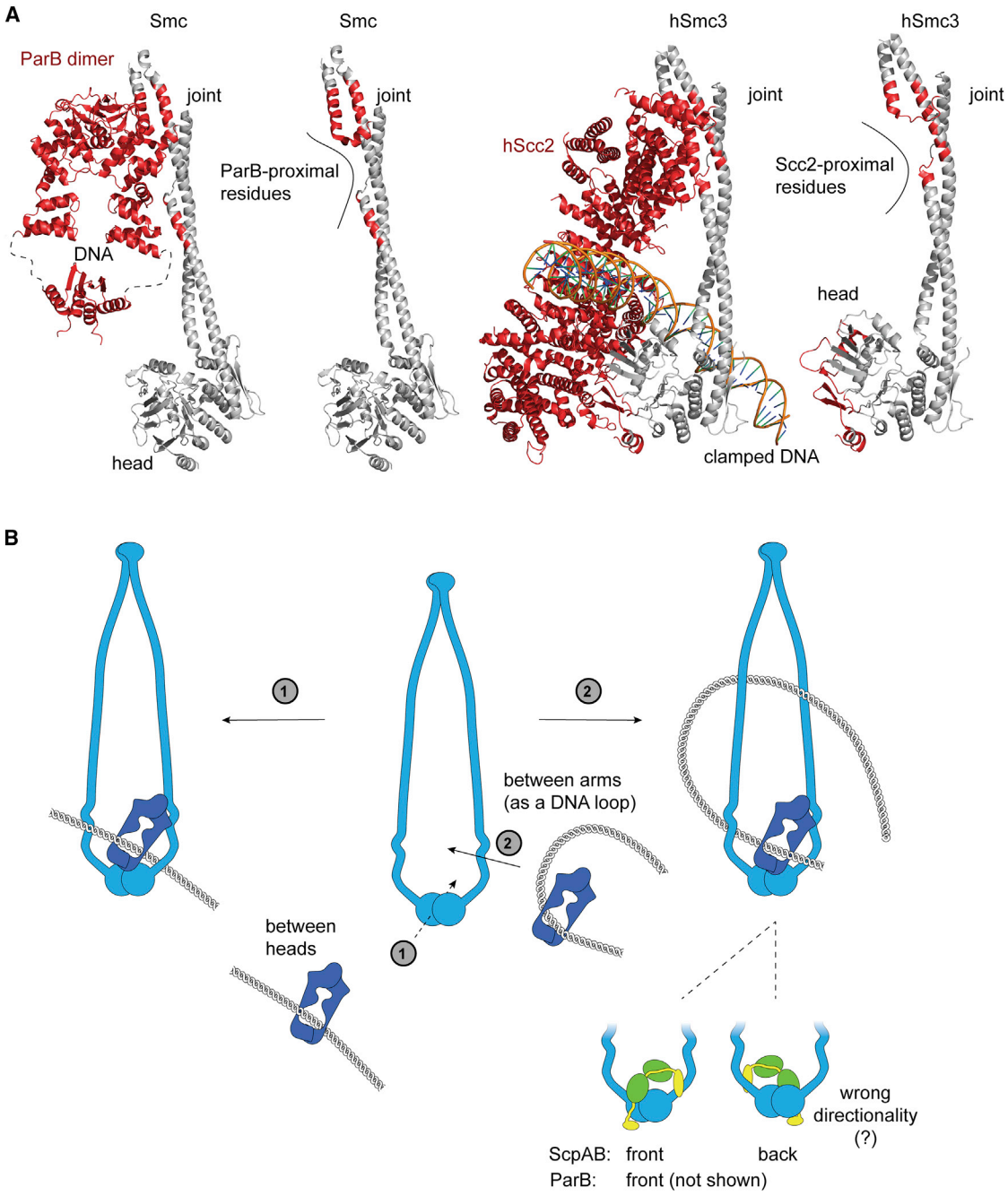

Figure 7. Structural similarities and models

(A) Comparison of the joint-ParB interface (left panels) and the Smc3 joint-Scc2 interface in human cohesin (right panels). ParB-proximal and Scc2-proximal residues on the Smc and Smc3 joint (C_α-C_α distance <10 Å), respectively, are indicated in red colors. The Scc2/DNA structure in ATP-engaged human cohesin is displayed (PDB: 6YUF) (right panel). Only the Smc3 and Scc2 subunits are shown for simplicity. For direct comparison, the SMC subunits are also displayed in isolation. Superimposition with MukB (PDB: 7NZ3) was omitted due to significant structural divergence of the respective joint domains (Bürmann et al., 2021).
(B) Putative models for the contact between ParB-clamped DNA and the Smc dimer. ScpAB is omitted from some representations for simplicity. Two scenarios are considered: DNA passage between disengaged heads ("1") and insertion of a DNA loop into the Smc interarm space ("2"), the product of which are shown on the left and right panels, respectively. ParB is shown to interact with the right Smc monomer (ParB in "front" of Smc). ScpAB can either associate on the same side ("front") or on the other side ("back"). Possible variations of these scenarios with pseudo-topological and non-topological modes of DNA association are not shown for the sake of simplicity. See also Figure S7.

side as ScpAB ("front") or approach from the opposite side ("back"). According to the DNA-segment-capture model, in the latter scenario, subsequent DNA translocation (without prior conversion to a topological DNA-Smc association—"loading") would shrink the newly captured DNA loop from the Smc complex and would thus be counterproductive (Diebold-Durand et al., 2017; Marko et al., 2019; Nomidis et al., 2022). However, results obtained with engineered asymmetric Smc dimers were not fully conclusive, possibly indicating that both scenarios may contribute to Smc targeting (Figures S7A and S7B). The inherent symmetry of the Smc and ParB dimers may even allow for the simultaneous engagement of two joint-ParB interfaces, thus possibly stabilizing the Smc-ParB association. Under the reasonable assumption that the ParB N-M architecture is relatively rigid (Soh et al., 2019), this is only possible after major reorganization of the Smc coiled coils requiring an X-shaped arrangement of the Smc proteins in the dimer (Figure S7C). Whether such an extreme coiled coil configuration occurs even transiently is doubtful. Another possibility is that a single ParB clamp recruits two Smc complexes, e.g., to build a dimeric motor complex for bidirectional translocation.

The ParB CTP binding domain

We show here that the N-terminal CTP-binding domain of ParB has a crucial role in the targeting of Smc to the chromosome. It is located farthest away from the ParB-clamped DNA, thus possibly reaching out from the partition complex to contact and capture free Smc dimers (Figure 7A). In close vicinity lies the unstructured N-terminal peptide of ParB that stimulates ParA ATP hydrolysis, potentially suggesting mutually exclusive binding of ParA and Smc and thus antagonistic regulation. These two ParB activities can now be uncoupled by separation-of-function mutations with ParB(L69S, K70E, E101K) specifically hindering Smc targeting and ParB(L5H) being defective in stimulating ParA ATP hydrolysis (Gruber and Errington, 2009). Notably, chromosome segregation via ParA requires ParB CTP hydrolysis, while Smc recruitment does not, indicating further opportunities for differential regulation (Antar et al., 2021). Moreover, recent findings indicate that ParA in turn controls Smc function, possibly at the DNA loading step (Roberts et al., 2021), altogether implying an elaborate network of regulation.

A transferable system for chromosome folding

We found that a module for chromosome segregation is remarkably robust. Together, the components taken from *S. pneumoniae* are able to promote chromosome segregation in the distantly related bacterium, *B. subtilis*, implying that direct binding to host factors (such as topoisomerases or nucleoid-associated proteins) is dispensable at least for all essential functions. Moreover, such host factors do not interfere with the basal activity of this module. Chromosome organization by Smc-ScpAB thus occurs unhindered on "foreign" chromosomal DNA. This implies, for example, that overcoming of obstacles on the DNA (during DNA loop extrusion) does not require dedicated bypass mechanisms (Anchimiuk et al., 2021; Brandao et al., 2021).

Mapping weak binding interfaces by gene transplantation and structure prediction

We initially aimed to detect the Smc-ParB interaction by performing biophysical interaction studies (including pull-down, coelution, anisotropy, and biolayer interferometry) using purified components and cofactors. However, our attempts were unsuccessful, possibly owing to a weak and transient nature of the association or the dependence on a so-far unknown cofactor or posttranslational modification. ParB self-concentrates to unusually high cellular concentrations within the partition complex (estimated to be as high as 10 mM at least for a plasmid ParB protein) (Guilhas et al., 2020), thus possibly bypassing the need for a high-affinity contact. The dissociation constant (K_D) for this interaction might be in the high μM or even mM range. Similar conditions are likely found in other systems. Our approach based on gene transplantation and cross-linking may be applicable to the study of weak interactions such as in biological condensates formed by liquid-liquid phase separation (Feng et al., 2019). When combined with structure prediction, this approach may be particularly powerful.

Limitations of the study

Our genetic approach driven by gene transplantation may have failed to uncover all ParB-Smc contacts promoting the recruitment of Smc-ScpAB to the chromosome. Consistent with this notion, the joint-ParB interface mutant shows residual Smc recruitment (Figure 6G). Moreover, the importance of this interface in more highly diverged bacteria remains to be established, and it remains unclear how the identified contact promotes Smc function. It may merely increase the local concentration of Smc or have an active role in Smc loading, such as presenting a DNA segment for capture by Smc-ScpAB. The nucleotide states of Smc and ParB in the Smc-ParB complex are also not fully established. Solving the structures of loading intermediates will likely shed further light on the loading reaction.

STAR★METHODS

Detailed methods are provided in the online version of this paper and include the following:

- KEY RESOURCES TABLE
- RESOURCE AVAILABILITY
  - Lead contact
  - Materials availability
  - Data and code availability
- EXPERIMENTAL MODEL AND SUBJECT DETAILS
  - *Bacillus* subtilis strains and growth conditions
- METHOD DETAILS
  - Strain construction
  - Viability assessment by dilution spotting
  - Protein extraction for immunoblotting
  - Immunoblotting
  - Chromosome conformation capture coupled with deep sequencing (3C-seq)
  - Sample collection
  - Cell pellet processing
  - DNA purification

SUPPLEMENTAL INFORMATION

Supplemental information can be found online at https://doi.org/10.1016/j.celrep.2022.111273.

ACKNOWLEDGMENTS

We are grateful to Frank Bürmann for comments on the manuscript and all members of the Gruber lab for stimulating discussions and feedback. We thank the Jan-Willem Veening lab for help with imaging and the Lausanne Genome Technologies Facility (GTF) for DNA sequencing. This work was supported by the Swiss National Science Foundation (197770 to S.G.) and the European Research Council (724482 to S.G.). H.W.L. is supported by an EMBO Postdoctoral fellowship (ALTF 490-2021).

AUTHOR CONTRIBUTIONS

Conceptualization, S.G. and F.P.B.; Methodology, M.L.D.D., F.P.B., A.A., and H.W.L.; Investigation, F.P.B., H.W.L., and A.A.; Writing – Original Draft, F.P.B. and S.G.; Writing – Review & Editing, all authors.; Funding Acquisition, S.G.; Resources, S.G.; Supervision, S.G.

DECLARATION OF INTERESTS

The authors declare no competing interests.

Received: January 5, 2022
Revised: June 21, 2022
Accepted: August 5, 2022
Published: August 30, 2022

REFERENCES

Anchimiuk, A., Lioy, V.S., Bock, F.P., Minnen, A., Boccard, F., and Gruber, S. (2021). A low Smc flux avoids collisions and facilitates chromosome organization in Bacillus subtilis. Elife *10*, e65467. https://doi.org/10.7554/eLife.65467.

Antar, H., Soh, Y.M., Zamuner, S., Bock, F.P., Anchimiuk, A., Rios, P.D.L., and Gruber, S. (2021). Relief of ParB autoinhibition by parS DNA catalysis and recycling of ParB by CTP hydrolysis promote bacterial centromere assembly. Sci. Adv. *7*, eabj2854. https://doi.org/10.1126/sciadv.abj2854.

Brandão, H.B., Ren, Z., Karaboja, X., Mirny, L.A., and Wang, X. (2021). DNA-loop-extruding SMC complexes can traverse one another in vivo. Nat. Struct. Mol. Biol. *28*, 642–651. https://doi.org/10.1038/s41594-021-00626-1.

Bürmann, F., Basfeld, A., Vazquez Nunez, R., Diebold-Durand, M.L., Wilhelm, L., and Gruber, S. (2017). Tuned SMC arms drive chromosomal loading of prokaryotic condensin. Mol. Cell *65*, 861–872.e9. https://doi.org/10.1016/j.molcel.2017.01.026.

Bürmann, F., Funke, L.F.H., Chin, J.W., and Löwe, J. (2021). Cryo-EM structure of MukBEF reveals DNA loop entrapment at chromosomal unloading sites. Mol. Cell *81*, 4891–4906.e8. https://doi.org/10.1016/j.molcel.2021.10.011.

Bürmann, F., and Gruber, S. (2015). SMC condensin: promoting cohesion of replicon arms. Nat. Struct. Mol. Biol. *22*, 653–655. https://doi.org/10.1038/nsmb.3082.

Bürmann, F., Shin, H.C., Basquin, J., Soh, Y.M., Giménez-Oya, V., Kim, Y.G., Oh, B.H., and Gruber, S. (2013). An asymmetric SMC-kleisin bridge in prokaryotic condensin. Nat. Struct. Mol. Biol. *20*, 371–379. https://doi.org/10.1038/nsmb.2488.

Chen, B.-W., Lin, M.-H., Chu, C.-H., Hsu, C.-E., and Sun, Y.-J. (2015). Insights into ParB spreading from the complex structure of Spo0J and *parS*. Proc. Natl. Acad. Sci. USA *112*, 6613–6618. https://doi.org/10.1073/pnas.1421927112.

Davidson, I.F., Bauer, B., Goetz, D., Tang, W., Wutz, G., and Peters, J.M. (2019). DNA loop extrusion by human cohesin. Science *366*, 1338–1345. https://doi.org/10.1126/science.aaz3418.

Diebold-Durand, M.L., Bürmann, F., and Gruber, S. (2019). High-throughput allelic replacement screening in Bacillus subtilis. Methods Mol. Biol. *2004*, 49–61. https://doi.org/10.1007/978-1-4939-9520-2_5.

Diebold-Durand, M.L., Lee, H., Ruiz Avila, L.B., Noh, H., Shin, H.C., Im, H., Bock, F.P., Bürmann, F., Durand, A., Basfeld, A., et al. (2017). Structure of full-length SMC and rearrangements required for chromosome organization. Mol. Cell *67*, 334–347.e5. https://doi.org/10.1016/j.molcel.2017.06.010.

Evans, R., O'Neill, M., Pritzel, A., Antropova, N., Senior, A., Green, T., Žídek, A., Bates, R., Blackwell, S., Yim, J., et al. (2021). Protein complex prediction with AlphaFold-Multimer. Preprint at bioRxiv. https://doi.org/10.1101/2021.10.04.463034.

Feng, Z., Chen, X., Wu, X., and Zhang, M. (2019). Formation of biological condensates via phase separation: characteristics, analytical methods, and physiological implications. J. Biol. Chem. *294*, 14823–14835. https://doi.org/10.1074/jbc.REV119.007895.

Fisher, G.L., Pastrana, C.L., Higman, V.A., Koh, A., Taylor, J.A., Butterer, A., Craggs, T., Sobott, F., Murray, H., Crump, M.P., et al. (2017). The structural basis for dynamic DNA binding and bridging interactions which condense the bacterial centromere. Elife *6*, e28086. https://doi.org/10.7554/eLife.28086.

Gligoris, T.G., Scheinost, J.C., Bürmann, F., Petela, N., Chan, K.L., Uluocak, P., Beckouët, F., Gruber, S., Nasmyth, K., and Löwe, J. (2014). Closing the cohesin ring: structure and function of its Smc3-kleisin interface. Science *346*, 963–967. https://doi.org/10.1126/science.1256917.

Gruber, S., and Errington, J. (2009). Recruitment of condensin to replication origin regions by ParB/SpoOJ promotes chromosome segregation in B. subtilis. Cell *137*, 685–696. https://doi.org/10.1016/j.cell.2009.02.035.

Gruber, S., Veening, J.W., Bach, J., Blettinger, M., Bramkamp, M., and Errington, J. (2014). Interlinked sister chromosomes arise in the absence of condensin during fast replication in B. subtilis. Curr. Biol. *24*, 293–298. https://doi.org/10.1016/j.cub.2013.12.049.

Guilhas, B., Walter, J.C., Rech, J., David, G., Walliser, N.O., Palmeri, J., Mathieu-Demaziere, C., Parmeggiani, A., Bouet, J.Y., Le Gall, A., and Nollmann, M. (2020). ATP-driven separation of liquid phase condensates in bacteria. Mol. Cell *79*, 293–303.e4. https://doi.org/10.1016/j.molcel.2020.06.034.

Haering, C.H., Löwe, J., Hochwagen, A., and Nasmyth, K. (2002). Molecular architecture of SMC proteins and the yeast cohesin complex. Mol. Cell *9*, 773–788. https://doi.org/10.1016/s1097-2765(02)00515-4.

Higashi, T.L., Eickhoff, P., Sousa, J.S., Locke, J., Nans, A., Flynn, H.R., Snijders, A.P., Papageorgiou, G., O'Reilly, N., Chen, Z.A., et al. (2020). A structure-based mechanism for DNA entry into the cohesin ring. Mol. Cell *79*, 917–933.e9. https://doi.org/10.1016/j.molcel.2020.07.013.

Hirano, M., and Hirano, T. (2002). Hinge-mediated dimerization of SMC protein is essential for its dynamic interaction with DNA. EMBO J. *21*, 5733–5744. https://doi.org/10.1093/emboj/cdf575.

Hwang, L.C., Vecchiarelli, A.G., Han, Y.W., Mizuuchi, M., Harada, Y., Funnell, B.E., and Mizuuchi, K. (2013). ParA-mediated plasmid partition driven by protein pattern self-organization. EMBO J. *32*, 1238–1249. https://doi.org/10.1038/emboj.2013.34.

Jalal, A.S.B., Tran, N.T., Wu, L.J., Ramakrishnan, K., Rejzek, M., Gobbato, G., Stevenson, C.E.M., Lawson, D.M., Errington, J., and Le, T.B.K. (2021). CTP

regulates membrane-binding activity of the nucleoid occlusion protein Noc. Mol. Cell *81*, 3623–3636.e6. https://doi.org/10.1016/j.molcel.2021.06.025.

Jumper, J., Evans, R., Pritzel, A., Green, T., Figurnov, M., Ronneberger, O., Tunyasuvunakool, K., Bates, R., Žídek, A., Potapenko, A., et al. (2021). Highly accurate protein structure prediction with AlphaFold. Nature *596*, 583–589. https://doi.org/10.1038/s41586-021-03819-2.

Käshammer, L., Saathoff, J.-H., Lammens, K., Gut, F., Bartho, J., Alt, A., Kessler, B., and Hopfner, K.-P. (2019). Mechanism of DNA end sensing and processing by the Mre11-rad50 complex. Mol. Cell *76*, 382–394.e6. https://doi.org/10.1016/j.molcel.2019.07.035.

Langmead, B., and Salzberg, S.L. (2012). Fast gapped-read alignment with Bowtie 2. Nat. Methods *9*, 357–359. https://doi.org/10.1038/nmeth.1923.

Lee, B.G., Rhodes, J., and Löwe, J. (2022). Clamping of DNA shuts the condensin neck gate. Proc. Natl. Acad. Sci. USA *119*, e2120006119. https://doi.org/10.1073/pnas.2120006119.

Leonard, T.A., Butler, P.J., and Löwe, J. (2005). Bacterial chromosome segregation: structure and DNA binding of the Soj dimer - a conserved biological switch. EMBO J. *24*, 270–282. https://doi.org/10.1038/sj.emboj.7600530.

Lim, H.C., Surovtsev, I.V., Beltran, B.G., Huang, F., Bewersdorf, J., and Jacobs-Wagner, C. (2014). Evidence for a DNA-relay mechanism in ParABS-mediated chromosome segregation. Elife *3*, e02758. https://doi.org/10.7554/eLife.02758.

Lioy, V.S., Cournac, A., Marbouty, M., Duigou, S., Mozziconacci, J., Espéli, O., Boccard, F., and Koszul, R. (2018). Multiscale structuring of the E. coli chromosome by nucleoid-associated and condensin proteins. Cell *172*, 771–783.e18. https://doi.org/10.1016/j.cell.2017.12.027.

Marko, J.F., De Los Rios, P., Barducci, A., and Gruber, S. (2019). DNA-segment-capture model for loop extrusion by structural maintenance of chromosome (SMC) protein complexes. Nucleic Acids Res. *47*, 6956–6972. https://doi.org/10.1093/nar/gkz497.

Minnen, A., Attaiech, L., Thon, M., Gruber, S., and Veening, J.W. (2011). SMC is recruited to oriC by ParB and promotes chromosome segregation in Streptococcus pneumoniae. Mol. Microbiol. *81*, 676–688. https://doi.org/10.1111/j.1365-2958.2011.07722.x.

Minnen, A., Bürmann, F., Wilhelm, L., Anchimiuk, A., Diebold-Durand, M.L., and Gruber, S. (2016). Control of smc coiled coil architecture by the ATPase heads facilitates targeting to chromosomal ParB/parS and release onto flanking DNA. Cell Rep. *14*, 2003–2016. https://doi.org/10.1016/j.celrep.2016.01.066.

Mirdita, M., Schütze, K., Moriwaki, Y., Heo, L., Ovchinnikov, S., and Steinegger, M. (2022). ColabFold: making protein folding accessible to all. Nat. Methods *19*, 679–682. https://doi.org/10.1038/s41592-022-01488-1.

Murray, H., and Errington, J. (2008). Dynamic control of the DNA replication initiation protein DnaA by Soj/ParA. Cell *135*, 74–84. https://doi.org/10.1016/j.cell.2008.07.044.

Nomidis, S.K., Carlon, E., Gruber, S., and Marko, J.F. (2022). DNA tension-modulated translocation and loop extrusion by SMC complexes revealed by molecular dynamics simulations. Nucleic Acids Res. *50*, 4974–4987. https://doi.org/10.1093/nar/gkac268.

Osorio-Valeriano, M., Altegoer, F., Das, C.K., Steinchen, W., Panis, G., Connolley, L., Giacomelli, G., Feddersen, H., Corrales-Guerrero, L., Giammarinaro, P.I., et al. (2021). The CTPase activity of ParB determines the size and dynamics of prokaryotic DNA partition complexes. Mol. Cell *81*, 3992–4007.e10. https://doi.org/10.1016/j.molcel.2021.09.004.

Palecek, J.J., and Gruber, S. (2015). Kite proteins: a superfamily of SMC/kleisin partners conserved across bacteria, archaea, and eukaryotes. Structure *23*, 2183–2190. https://doi.org/10.1016/j.str.2015.10.004.

Panas, M.W., Jain, P., Yang, H., Mitra, S., Biswas, D., Wattam, A.R., Letvin, N.L., and Jacobs, W.R., Jr. (2014). Noncanonical SMC protein in Mycobacterium smegmatis restricts maintenance of Mycobacterium fortuitum plasmids. Proc. Natl. Acad. Sci. USA *111*, 13264–13271. https://doi.org/10.1073/pnas.1414207111.

Petrushenko, Z.M., She, W., and Rybenkov, V.V. (2011). A new family of bacterial condensins. Mol. Microbiol. *81*, 881–896. https://doi.org/10.1111/j.1365-2958.2011.07763.x.

Prince, J.P., Bolla, J.R., Fisher, G.L.M., Mäkelä, J., Fournier, M., Robinson, C.V., Arciszewska, L.K., and Sherratt, D.J. (2021). Acyl carrier protein promotes MukBEF action in Escherichia coli chromosome organization-segregation. Nat. Commun. *12*, 6721. https://doi.org/10.1038/s41467-021-27107-9.

Quisel, J.D., and Grossman, A.D. (2000). Control of sporulation gene expression in Bacillus subtilis by the chromosome partitioning proteins Soj (ParA) and Spo0J (ParB). J. Bacteriol. *182*, 3446–3451. https://doi.org/10.1128/JB.182.12.3446-3451.2000.

Roberts, D.M., Anchimiuk, A., Kloosterman, T.G., Murray, H., Wu, L.J., Gruber, S., and Errington, J. (2021). Chromosome remodelling by SMC/Condensin in *B. subtilis* is regulated by Soj/ParA during growth and sporulation. Preprint at bioRxiv. https://doi.org/10.1101/2021.12.18.473321.

Schindelin, J., Arganda-Carreras, I., Frise, E., Kaynig, V., Longair, M., Pietzsch, T., Preibisch, S., Rueden, C., Saalfeld, S., Schmid, B., et al. (2012). Fiji: an open-source platform for biological-image analysis. Nat. Methods *9*, 676–682. https://doi.org/10.1038/nmeth.2019.

Scholefield, G., Whiting, R., Errington, J., and Murray, H. (2011). Spo0J regulates the oligomeric state of Soj to trigger its switch from an activator to an inhibitor of DNA replication initiation. Mol. Microbiol. *79*, 1089–1100. https://doi.org/10.1111/j.1365-2958.2010.07507.x.

Schumacher, M.A., and Funnell, B.E. (2005). Structures of ParB bound to DNA reveal mechanism of partition complex formation. Nature *438*, 516–519. https://doi.org/10.1038/nature04149.

Shaltiel, I.A., Datta, S., Lecomte, L., Hassler, M., Kschonsak, M., Bravo, S., Stober, C., Ormanns, J., Eustermann, S., and Haering, C.H. (2022). A hold-and-feed mechanism drives directional DNA loop extrusion by condensin. Science *376*, 1087–1094. https://doi.org/10.1126/science.abm4012.

Shi, Z., Gao, H., Bai, X.C., and Yu, H. (2020). Cryo-EM structure of the human cohesin-NIPBL-DNA complex. Science *368*, 1454–1459. https://doi.org/10.1126/science.abb0981.

Soh, Y.M., Davidson, I.F., Zamuner, S., Basquin, J., Bock, F.P., Taschner, M., Veening, J.W., De Los Rios, P., Peters, J.M., and Gruber, S. (2019). Self-organization of parS centromeres by the ParB CTP hydrolase. Science *366*, 1129–1133. https://doi.org/10.1126/science.aay3965.

Sullivan, N.L., Marquis, K.A., and Rudner, D.Z. (2009). Recruitment of SMC by ParB-parS organizes the origin region and promotes efficient chromosome segregation. Cell *137*, 697–707. https://doi.org/10.1016/j.cell.2009.04.044.

Surtees, J.A., and Funnell, B.E. (2001). The DNA binding domains of P1 ParB and the architecture of the P1 plasmid partition complex. J. Biol. Chem. *276*, 12385–12394. https://doi.org/10.1074/jbc.M009370200.

Tišma, M., Panoukidou, M., Antar, H., Soh, Y.M., Barth, R., Pradhan, B., Barth, A., van der Torre, J., Michieletto, D., Gruber, S., and Dekker, C. (2022). ParB proteins can bypass DNA-bound roadblocks via dimer-dimer recruitment. Sci. Adv. *8*, eabn3299. https://doi.org/10.1126/sciadv.abn3299.

Tran, N.T., Laub, M.T., and Le, T.B.K. (2017). SMC progressively aligns chromosomal arms in Caulobacter crescentus but is antagonized by convergent transcription. Cell Rep. *20*, 2057–2071. https://doi.org/10.1016/j.celrep.2017.08.026.

Vazquez Nunez, R., Polyhach, Y., Soh, Y.M., Jeschke, G., and Gruber, S. (2021). Gradual opening of Smc arms in prokaryotic condensin. Cell Rep. *35*, 109051. https://doi.org/10.1016/j.celrep.2021.109051.

Vazquez Nunez, R., Ruiz Avila, L.B., and Gruber, S. (2019). Transient DNA occupancy of the SMC interarm space in prokaryotic condensin. Mol. Cell *75*, 209–223.e6. https://doi.org/10.1016/j.molcel.2019.05.001.

Wang, X., Brandão, H.B., Le, T.B.K., Laub, M.T., and Rudner, D.Z. (2017). Bacillus subtilis SMC complexes juxtapose chromosome arms as they travel from origin to terminus. Science *355*, 524–527. https://doi.org/10.1126/science.aai8982.

Wilhelm, L., Bürmann, F., Minnen, A., Shin, H.C., Toseland, C.P., Oh, B.H., and Gruber, S. (2015). SMC condensin entraps chromosomal DNA by an ATP

hydrolysis dependent loading mechanism in Bacillus subtilis. Elife *4*. https://doi.org/10.7554/eLife.06659.

Yatskevich, S., Rhodes, J., and Nasmyth, K. (2019). Organization of chromosomal DNA by SMC complexes. Annu. Rev. Genet. *53*, 445–482. https://doi.org/10.1146/annurev-genet-112618-043633.

Yoshinaga, M., and Inagaki, Y. (2021). Ubiquity and origins of structural maintenance of chromosomes (SMC) proteins in eukaryotes. Genome Biol. Evol. *13*, evab256. https://doi.org/10.1093/gbe/evab256.

Zhang, H., and Schumacher, M.A. (2017). Structures of partition protein ParA with nonspecific DNA and ParB effector reveal molecular insights into principles governing Walker-box DNA segregation. Genes Dev. *31*, 481–492. https://doi.org/10.1101/gad.296319.117.

Zhao, S., and Fernald, R.D. (2005). Comprehensive algorithm for quantitative real-time polymerase chain reaction. J. Comput. Biol. *12*, 1047–1064. https://doi.org/10.1089/cmb.2005.12.1047.

STAR★METHODS

KEY RESOURCES TABLE

REAGENT or RESOURCE	SOURCE	IDENTIFIER
Antibodies		
Anti-ParB (Rabbit polyclonal)	David Rudner Lab	N/A
Anti-ScpB (Rabbit polyclonal)	Custom made - Eurogentec	N/A
Anti-GFP (Rabbit polyclonal)	Thermo Scientific	Cat# A-6455
Chemicals, peptides, and recombinant proteins		
Bis(maleimido)ethane (BMOE)	Thermo Scientific	Cat# 22323
Breathe-Easy sealing film	Diversified Biotech	Cat# BEM-1
BsaI	New England Biolabs	Cat# R0559L
Dynabeads Protein-G	Thermo Scientific	Cat# 10004D
Erythromycin	AppliChem	Cat# A2275,0005
GlycoBlue Coprecipitant	Ambion	Cat# AM9515
HaloTag-TMR Ligand	Promega	Cat# G8251
Lysozyme from Chicken Egg White	Merck	Cat# L6876-5G
NuPAGE LDS Sample Buffer (4X)	Thermo Scientific	Cat# NP0008
Protease Inhibitor Cocktail	Merck	Cat# P8849-5ML
Ready-Lyse Lysozyme Solution	Epicenter	Cat# R1802M
RNase A	Merck	Cat# R5125
Sm Nuclease	Core Facility	N/A
T4 DNA Ligase	Thermo Scientific	Cat# EL0016
Trichloroacetic acid (TCA)	Merck	Cat# T6399
Glass beads (100μm)	Merck	Cat# G6469
1,4-Dithiothreitol (DTT)	BioChemica	Cat# A1101.0025
AMPure XP reagent	Beckman Coulter	Cat# A63880
HpaII	New England Biolabs	Cat# R0171L
Proteinase K	Eurobio	Cat# GEXPRK01-B5
Benzonase	Merck	Cat# E1014
Formaldehyde solution	Merck	Cat# 252549
SMCC	Thermo Scientific	Cat# 22360
Phenol	Merck	Cat# P4557
Chloroform	Carlo Erba	Cat# P02410 × 10^{16}
Critical commercial assays		
Takyon SYBR 2xMasterMix Blue dTTP No ROX	Eurogentec	Cat# UF-NSMT-B0701
Novex 4-12% Tris-Glycine Mini Gels	Thermo Scientific	Cat# XP04125BOX
NuPAGE 3-8% Tris-Acetate Gels	Thermo Scientific	Cat# EA03755BOX
QIAquick PCR Purification Kit	QIAGEN	Cat# 28106
Deposited data		
Original data	Mendeley Data	https://doi.org/10.17632/yn5rbmsj9x.1
3C-Seq Data	NCBI GEO database	GSE190491
ChIP-Seq Data	NCBI GEO database	GSE206446
Experimental models: Organisms/strains		
B. subtilis strains, see Tables S1 and S2	Gruber Lab	N/A
Oligonucleotides		
For qPCR oligonucleotides, see Table S3	N/A	N/A

(*Continued on next page*)

Continued

REAGENT or RESOURCE	SOURCE	IDENTIFIER
Software and algorithms		
Real-Time PCR Miner	Zhao and Fernald, 2005	http://ewindup.info/miner/
ImageQuant TL 1D V8.1	GE Healthcare	http://www.gelifesciences.com/en/us/shop/protein-analysis/molecular-imaging-for-proteins/imaging-software/imagequant-tl-8-1-p-00110
AlphaFold2	Mirdita et al., 2022	https://colab.research.google.com/github/sokrypton/ColabFold/blob/main/beta/AlphaFold2_advanced.ipynb
Leica Application Suite X (LAS X)	Leica	N/A
MATLAB (R2019b)	MathWorks	N/A
FUSION FX imaging software	Vilber	N/A
Seqmonk	Babraham Bioinfomatics	N/A
FIJI	Schindelin et al., 2012	N/A

RESOURCE AVAILABILITY

Lead contact

Further information and requests for resources and reagents should be directed to and will be fulfilled by the Lead Contact, Stephan Gruber (stephan.gruber@unil.ch).

Materials availability

All DNA constructs and strains generated in this study are available from the lead contact without restriction.

Data and code availability

- Raw sequencing data obtained in this work can be found at the gene expression omnibus (accession number for 3C-Seq data: GEO: GSE190491 and for ChIP-Seq data: GEO: GSE206446). All other raw data are available via Mendeley Data: https://doi.org/10.17632/yn5rbmsj9x.1.
- This paper does not report original code.
- Any additional information required to reanalyze the data reported in this paper is available from the lead contact upon request.

EXPERIMENTAL MODEL AND SUBJECT DETAILS

Bacillus subtilis strains and growth conditions

The *B. subtilis* strains utilized in this work originate from the 1A700 isolate. A list of strains and genotypes is given in Table S1. The assignment of strains to figure panels is listed in Table S2. Strains were selected and maintained on SMG (SMM solution, glucose, glutamate, tryptophan) agar plates under appropriate antibiotic selection at 37°C (Diebold-Durand et al., 2019). Liquid cultures were inoculated from SMG agar plates in SMG medium or Luria-Bertani (LB) broth and grown at 37°C under constant agitation. Growth in rich medium was evaluated by spotting onto ONA (Oxoid nutrient) agar plates.

METHOD DETAILS

Strain construction

Transformation with recombinant DNA was used to engineer *B. subtilis* strains at the *smc*, *scpAB*, *parAB* and *amyE* loci by allelic replacement using natural competence induced by starvation under standard conditions (1-2 h incubation in SMM medium lacking amino acid supplements) as also described in (Diebold-Durand et al., 2019). Strains were selected on SMG-agar plates under appropriate antibiotic selection at 37°C. Genotypes were verified for selected single colony isolates by antibiotic resistance profiling, colony PCR, and Sanger sequencing as required.

Viability assessment by dilution spotting

Cultures were inoculated in SMG medium and grown for 8 h at 37°C under constant agitation. Cultures were diluted 1:9 in series. Dilutions of 9^2 and 9^5 were spotted on SMG-agar and ONA-agar plates and grown at 37°C. Colony growth was documented by imaging after 16 h for ONA-agar plates and 24 h for SMG-agar plates.

Protein extraction for immunoblotting

Bacillus subtilis cells were cultured in SMG at 37°C until mid-exponential phase (OD600 = 0.02–0.03), where they were pelleted and resuspended in 10% (w/v) trichloroacetic acid (TCA, Sigma) in 2 mL bead beater tubes. To lyse cells, 100μm glass beads (Sigma) were added to the resuspension which was then beaten with a FastPrep homogenizer (MP Biomedicals) for two 45-s cycles. The extract was pelleted and resuspended in 50μL LPS +200mM DTT. Samples were then pH-adjusted by adding 20μL 1M Tris base.

Immunoblotting

Protein samples were denatured for 2 min at 95°C, separated by SDS-polyacrylamide gel electrophoresis before transfer to nitrocellulose membranes. Chemiluminescence was visualized using ECL reagents via a Vilber FUSION imaging system.

Chromosome conformation capture coupled with deep sequencing (3C-seq)

3C-seq was performed essentially as described in (Anchimiuk et al., 2021). The maps obtained from two biological replicates were highly similar. The sequencing data are available at the NCBI GEO database under the accession: GSE190491.

Sample collection

Cultures were grown in SMG at 37°C in mid-exponential phase (OD600 = 0.02–0.03) and fixed with formaldehyde (3% final concentration) for 30 min at RT and 30 min at 4°C. Formaldehyde crosslinking was quenched by 30 min incubation with 0.25 M glycine at 4°C. Finally, the cells were pelleted by filtration, washed with fresh SMG and frozen in liquid nitrogen for storage at −80°C.

Cell pellet processing

To lyse the cells, 3C cell pellets were resuspended in 600 μL 1× TE (Sigma) supplemented with 4 μL of Ready-Lysozyme (35 U/μL, Tebu Bio). After 20 min incubation at RT, SDS was added to a final concentration of 0.5% and incubated for an additional 10 min. Fifty microliters of lysed cells were aliquoted into 8 tubes containing 450 μL of digestion mix (1× NEB 1 buffer, 1% Triton X-100, and 100 U HpaII enzyme [NEB]) and incubated at 37°C for 3 h with constant shaking. Fragmented DNA was collected by centrifugation, resuspended in 800 μL 1× TE and diluted into 4 tubes containing 8 mL of ligation mix (1× ligation buffer: 50 mM Tris-HCl, 10 mM MgCl2, 10 mM DTT, 1 mM ATP, 0.1 mg/mL BSA, 125 U T4 DNA ligase 5 U/mL) and incubated at 16°C for 4 h. The proximity ligation reaction was followed by O/N decrosslinking at 65°C in the presence of 250 μg/mL proteinase K (Eurobio) and 5 mM EDTA (Sigma).

DNA purification

To purify the DNA, isopropanol precipitation was performed. Each sample was mixed with 1 volume of isopropanol and 0.1 volume of 3 M NaOAc (pH 5.2, Sigma) and incubated at −80°C for 1 h. The DNA was collected by centrifugation and resuspended in 400 μL 1× TE at 30°C for 20 min. Next, phenol-chloroform-isoamyl alcohol extraction was performed, followed by final DNA precipitation using 1.5 volume of cold 100% EtOH in the presence of 0.1 volume of 3M NaOAc at −80°C for 30 min. Collected pellets were resuspended in 30 μL 1 × TE and incubated with RNaseA at 37°C for 30 min. All tubes belonging to the same sample were pooled, and the resulting 3C library was quantified on gel using ImageJ.

Library preparation and sequencing

All 3C libraries were adjusted to 1 μg for library preparation. Each 3C library volume was adjusted to 130 μL and sonicated using Covaris S220 following 500 bp target size recommendations from the manufacturer. Fragmented DNA was purified using a Qiagen PCR purification kit, eluted in 40 μL EB and quantified using a NanoDrop. Custom-made adapters were used to prepare the libraries for paired-end Illumina sequencing using ∼1 μg of DNA as an input. Adapter ligation was performed for 4 h at RT, followed by an inactivation step at 65°C for 20 min. DNA was purified with 0.75× AMPure beads, and 3 μL was used for 50 μL PCR (12 cycles). Amplified libraries were purified on Qiagen columns and paired-end sequenced on an Illumina platform (HiSeq4000 or NextSeq).

Processing of PE reads and generation of contact maps

A custom script was used to demultiplex the sequencing data. Prinseq was used to clean the data prior to processing it following the steps described at https://github.com/axelcournac/3C_tutorial. Briefly, each mate was mapped to the reference genome (NC_000964.3) using bowtie2 in very-sensitive-local mode. Next, data were sorted and both mates merged. The reads of mapping quality above 30 were filtered out and assigned to a restriction fragment. Uninformative events including recircularization on itself (loops), uncut fragments, and religations in the original orientation were discarded. Only pairs of reads corresponding to long-range interactions were used for the generation of contact maps (between 5 and 8% of all reads). A bin size of 10 kb was used. Contact

maps were normalized through the sequential component normalization procedure (SCN). Subsequent visualization was performed using MATLAB (R2019b). To facilitate visualization of the contact maps, first, the log10 and then a Gaussian filter (H = 1) were applied to smooth the image.

Live cell imaging

Cells were grown in SMG to OD600 = 0.04. Two milliliters of culture volume was spun down at 8000 rcf for 2 min at RT. The supernatant was removed, and the cells were resuspended in 10 μL PBS. Cell suspensions (0.5 μL) were spotted onto homemade agarose microscopy slides. Images were acquired using a Leica DMi8 microscope with an sCMOS DFC9000 (Leica) camera, a SOLA light engine (Lumencor) and a ×100/1.40 oil-immersion objective. Images were acquired with 600 ms exposure at 470 nm excitation and 520 nm emission. Images were processed using LasX v.3.3.0.16799 (Leica).

Chromatin immunoprecipitation (ChIP)

ChIP samples were prepared as described previously (Bürmann et al., 2017). Cultures were grown in 200 mL volumes SMG at 37°C. Cells were grown to mid-exponential phase (OD600 = 0.02–0.03) and fixed by incubation for 30 min with 1/10 [v/v] buffer F (50 mM Tris-HCl pH 7.4, 100 mM NaCl, 0.5 mM EGTA pH 8.0, 1 mM EDTA pH 8.0, 10% [w/v] formaldehyde). Cells were harvested by filtration and washed in cold PBS. The OD600 values of the samples were normalized to 2 and resuspended in TSEMS (50 mM Tris pH 7.4, 50 mM NaCl, 10 mM EDTA pH 8.0, 0.5 M sucrose and PIC (Sigma)) supplemented with 6 mg/mL chicken egg white lysozyme (Sigma). Samples were incubated at 37°C for 30 min under shaking. The resulting protoplasts were harvested by centrifugation, washed in 2 mL TSEMS, resuspended in ml TSEMS and split into 3 aliquots of equivalent volume before pelleting and flash freezing.

Samples were resuspended in 2 mL of buffer L (50 mM HEPES-KOH pH 7.5, 140 mM NaCl, 1 mM EDTA pH 8.0, 1% [v/v] Triton X-100, 0.1% [w/v] Na-deoxycholate, 0.1 mg/mL RNaseA and PIC (Sigma)), transferred to 5 mL round-bottom tubes and sonicated three times for 20 seconds using a Bandelin Sonoplus with an MS72 tip (90% pulse and 35% power output). Suspensions were centrifuged for 10 minutes at 21 krcf at 4°C. Samples were split into 200 μL input material and 800 μL IP material.

Antibody serum was incubated with equivalent volumes of Dynabeads Protein G suspension (Invitrogen) for 2 h at 4°C under gentle agitation. Beads were washed in 1 mL Buffer L directly prior to use and resuspended as 50 μL aliquots of 30 mg/mL. IP material was mixed with these 50 μL aliquots and incubated at 4°C for 2 hours under rotation. Bound material was subsequently washed by 1 mL washes with buffer L, L5 buffer L containing 500 mM NaCl), buffer W (10 mM Tris-HCl pH 8.0, 250 mM LiCl, 0.5% [v/v] NP-40, 0.5% [w/v] Na-deoxycholate, 1 mM EDTA pH 8.0) and buffer TE (10 mM Tris-HCl pH 8.0, 1 mM EDTA pH 8.0). Beads were resuspended in 520 μL TES (50 mM Tris-HCl pH 8.0, 10 mM EDTA pH 8.0, 1% (w/v) SDS). Input material was supplemented with 300 μL TES and 20 μL 10% SDS. Tubes were incubated at 65°C overnight under vigorous shaking.

DNA was purified using phenol-chloroform extraction by adding and thoroughly mixing first with 500 μL phenol equilibrated with buffer (10 mM Tris-HCl pH 8.0, 1 mM EDTA). Phases were separated by centrifugation for 10 min at 21 krcf. A total of 450 μL supernatant was subsequently mixed and again separated from 450 μL chloroform. Then, 400 μL supernatant was removed and mixed with 1.2 μL GlycoBlue (Invitrogen), 30 μL of 3 M Na-acetate (pH 5.2) and 1 mL ethanol (filtered). Samples were incubated at −20°C for at least 30 min. DNA was precipitated by centrifugation at room temperature with 21 krcf for 10 min. DNA was resuspended in 100 μL volumes of PB (Qiagen) and dissolved by incubation at 55°C under vigorous shaking for 10 minutes. Samples were subsequently purified using a PCR purification kit (Qiagen) as per protocol and eluted in 50 μL elution buffer.

For quantification by qPCR, samples were diluted to 1:10 for IP and 1:100 for input material. Reactions for qPCR were prepared by mixing 4 μL diluted samples with 5 μL 2 × 5 μL Takyon SYBR MasterMix and 1 μL qPCR primer mixture (3 μM). A list of qPCR primers is given in Table S3. Samples were run in a Rotor-Gene Q (Qiagen) and analyzed using PCR miner (Zhao and Fernald, 2005).

For deep sequencing, DNA libraries were prepared by Genomic Technologies Facility at CIG, UNIL, Lausanne. Briefly, the DNA was fragmented by sonication (Covaris S2). DNA libraries were prepared using the Ovation Ultralow Library Systems V2 Kit (NuGEN) with 15 cycles of PCR amplification. 20-30 million paired end sequence reads were obtained on a HiSeq4000 (Illumina) with 150 bp read length.

In vivo Cys-Cys and Lys-Cys cross-linking

Cross-linking was performed as described in (Soh et al., 2019). Cultures were grown in SMG to OD600 of 0.03–0.04 at 37°C. Cells were mixed with ice and harvested by centrifugation. Sample handling and preparation were performed on ice and cold at every step. Cells were washed in PBSG (PBS with 0.1% [v/v] glycerol). Samples were resuspended in 1 mL PBSG. 1.25 OD600 equivalents were taken and pelleted by centrifugation. Pellets were resuspended in 30 μL PBSG. Cross-linking agent (SMCC (Thermo) or BMOE (Thermo) was added to a final concentration of 0.5 mM and mixed by vortexing. Reactions were incubated on ice for 10 minutes and then quenched by the addition of 0.5 mM final concentration 2-mercaptoethanol with subsequent incubation for 2 minutes. Samples were supplemented with additives at the indicated final concentrations: benzonase (750 U/mL; Sigma), 5 μM HaloTag-TMR ligand (Promega), Ready-Lyse Lysozyme (47 U/μL; Epicentre), and 1× PIC (Sigma-Aldrich). Samples were incubated at 37°C for 30 minutes under light protection. Samples were supplemented with LPS loading dye and denatured at 70°C for 5 minutes. Samples were run on 3-8% Tris-acetate gels (Invitrogen) at a constant power output of 35 mA at 4°C. In-gel fluorescence was imaged using an Amersham Typhoon (GE Healthcare) with a Cy3 DIGE filter. Quantification was performed using ImageQuant (GE Healthcare).

Structure prediction by AlphaFold-Multimer

Predictions were performed using standard settings and databases for AlphaFold-Multimer via the Colab notebook (https://dpmd.ai/alphafold-colab) (with two predictions yielding virtually identical outcomes on 08 Nov 2021 and 06 Jun 2022) (Evans et al., 2021; Jumper et al., 2021; Mirdita et al., 2022). Sequences corresponding to previously crystallized fragments of *Bsu* Smc (Smc joint: PDB: 5NMO) and ParB (ParB domains N and M: PDB: 6SDK) were used as input to predict a 1:1 complex (Diebold-Durand et al., 2017; Soh et al., 2019). The coordinates of the predicted model and the predicted aligned error file are available as supplemental files (Supplementary file 1 and Supplementary file 2). Some predictions with larger sequence fragments or sequences of different origin gave comparable results.

QUANTIFICATION AND STATISTICAL ANALYSIS

Deep-sequencing data analysis

Deep-sequencing data from ChIP or input samples were mapped to the *Bsu* reference genome NC_000964 (centered on its first coordinate) using Bowtie for Illumina in the Galaxy project website (https://usegalaxy.org/) (Langmead and Salzberg, 2012). Reads were filtered for mapping quality (MAPQ) greater than 10, reduced to bins of 1000 bp, and normalized for total read count in SeqMonk. Ratiometric analyses were performed as previously described (Vazquez Nunez et al., 2019). Briefly, the reduced data for each sample was compared to that of wild-type, and the larger of the two values was divided by the smaller. The resulting ratio was plotted above the coordinate axis for value (mutant) $\geq$ value (WT) and below the axis otherwise. The data were exported and visualized in Graphpad Prism 9. We obtained highly similar ChIP-seq maps for two biological replicates. The sequencing data are available at the NCBI GEO database under the accession: GSE206446.

Analysis of cross-linking efficiencies

Fluorescence intensities of Smc-HT bands were measured using ImageQuant TL 1D V8.1. Lanes were manually defined. After automated band detection background was corrected the Rolling Ball algorithm with a ball radius set to 129. Relative values were exported to R for calculation of fraction content per band.

Analysis of qPCR data

Threshold cycle (CT) was obtained by analyzing the fluorescence raw data in the Real-Time PCR Miner server (http://ewindup.info/miner/) (Zhao and Fernald, 2005). IP/input ratios were calculated as $\propto 2^{\Delta CT}$, where ΔCT = CT (Input) – CT and $\propto$ is a constant determined by extraction volumes and sample dilutions.

Cell Reports, Volume *40*

Supplemental information

A joint-ParB interface promotes Smc DNA recruitment

Florian P. Bock, Hon Wing Liu, Anna Anchimiuk, Marie-Laure Diebold-Durand, and Stephan Gruber

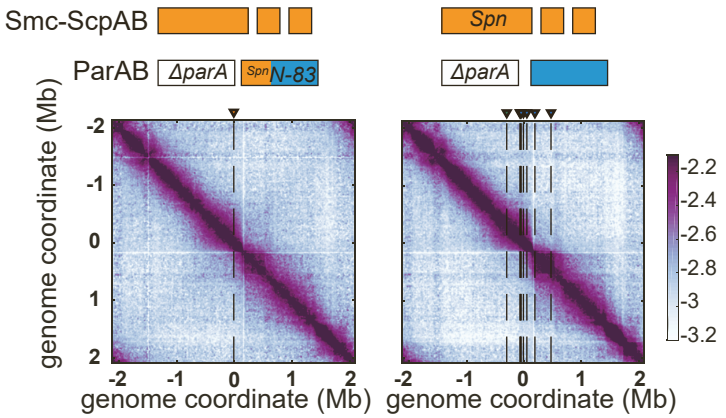

Figure S1. Additional 3C-Seq maps. Related to Figure 1.

Normalized 3C-seq contact maps of strains with the indicated genotypes (lacking some of the *parS* sites or *parA*) grown exponentially, display as in Figure 1C. Maps obtained from biological duplicates gave comparable results.

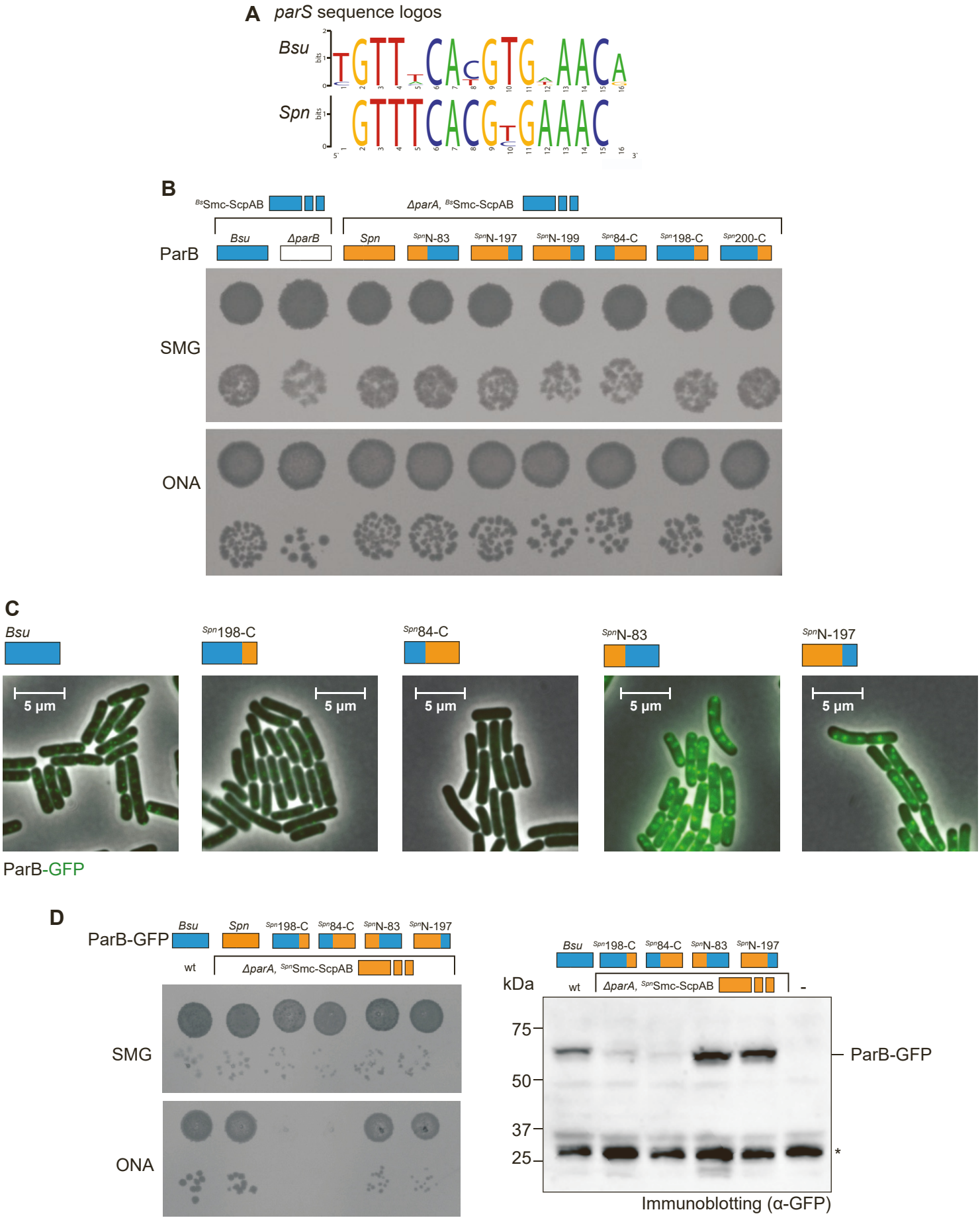
A parS sequence logos
Bsu
Spn
B
BsSmc-ScpAB
ΔparA, BsSmc-ScpAB
Bsu
ΔparB
Spn
SpnN-83
SpnN-197
SpnN-199
Spn84-C
Spn198-C
Spn200-C
ParB
SMG
ONA
C
Bsu
Spn198-C
Spn84-C
SpnN-83
SpnN-197
5 µm
ParB-GFP
D
ParB-GFP
Bsu
Spn
Spn198-C
Spn84-C
SpnN-83
SpnN-197
wt
ΔparA, SpnSmc-ScpAB
SMG
ONA
kDa
75
50
37
25
ParB-GFP
*
Immunoblotting (α-GFP)

Figure S2

Figure S2. GFP-tagged chimeric constructs are expressed in *B. subtilis*. Related to Figure 2.

A) Sequence logo for *Bsu* and *Spn parS* sites. B**)** Viability of cells harboring different *Bsu*/*Spn* chimeric ParB sequences in an otherwise wild-type strain background. Display as in Figure 1B. **C)** Microscopic image of *B. subtilis* cells containing different chimeric ParB proteins fused to GFP. As in Figure 2C. **D)** Left panel: viability of cells harboring different *Bsu*/*Spn* chimeric ParB sequences tagged with GFP. Right panel: Immunoblotting to estimate the cellular expression levels of *Bsu*/*Spn* chimeric GFP-tagged ParB proteins using antiserum raised against GFP.

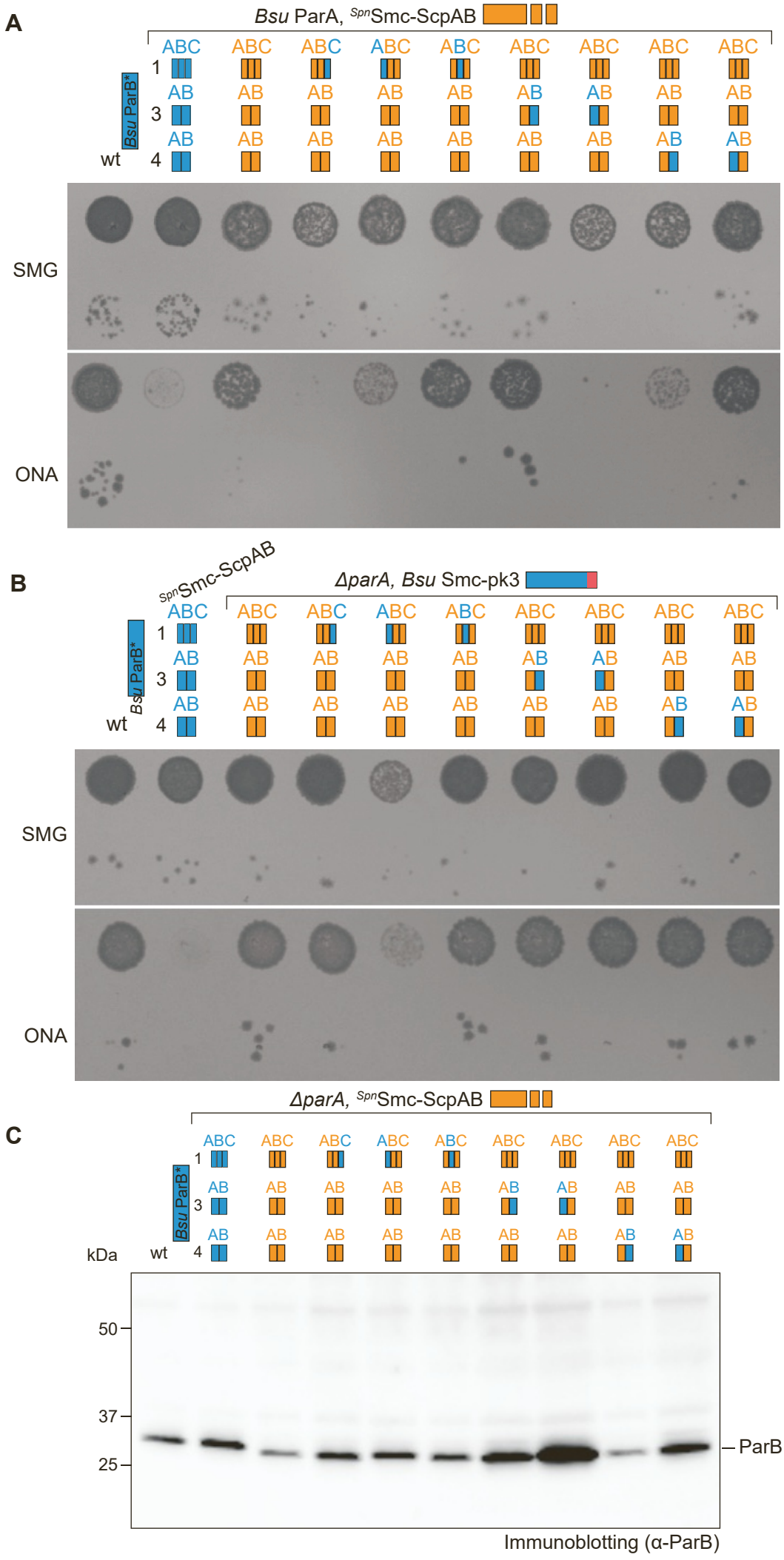
A
Bsu ParA, SpnSmc-ScpAB
Bsu ParB*
wt
1
3
4
ABC
AB
SMG
ONA
B
SpnSmc-ScpAB
ΔparA, Bsu Smc-pk3
C
ΔparA, SpnSmc-ScpAB
kDa
50
37
25
ParB
Immunoblotting (α-ParB)

Figure S3

Figure S3. Mapping of ParB residues involved in Smc interaction. Related to Figure 3.

A) Spotting assay of strains carrying ^{Spn}Smc-ScpAB, ParB chimeras and intact *parA* genes. As in Figure 3C but with ParA protein being present. **B)** Spotting assay of strains carrying the ^{Bsu}*smc-pk3* allele as well as a *parA* deletion and ParB chimeras as indicated. **C)** Immunoblotting to expression levels of *Bsu*/*Spn* chimeric ParB proteins using antiserum raised against ParB.

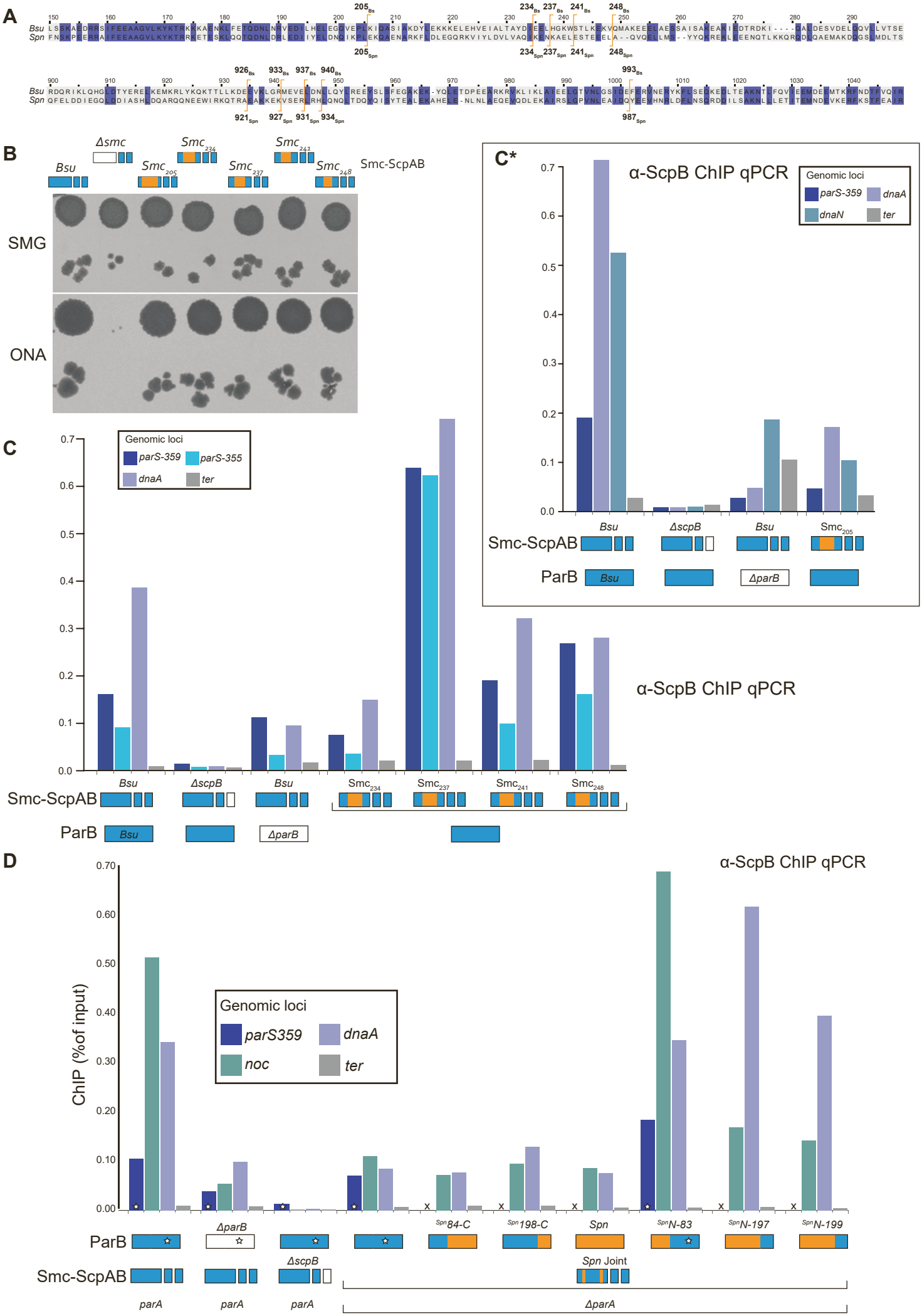
A
Bsu
Spn
B
Δsmc
Smc234
Smc241
Bsu
Smc205
Smc237
Smc248
Smc-ScpAB
SMG
ONA
C*
α-ScpB ChIP qPCR
Genomic loci
parS-359
dnaA
dnaN
ter
Bsu
ΔscpB
Bsu
Smc205
Smc-ScpAB
ParB
Bsu
ΔparB
C
Genomic loci
parS-359
parS-355
dnaA
ter
α-ScpB ChIP qPCR
Bsu
ΔscpB
Bsu
Smc234
Smc237
Smc241
Smc248
Smc-ScpAB
ParB
Bsu
ΔparB
D
α-ScpB ChIP qPCR
ChIP (%of input)
Genomic loci
parS359
dnaA
noc
ter
ΔparB
ΔscpB
Spn84-C
Spn198-C
Spn
SpnN-83
SpnN-197
SpnN-199
ParB
Smc-ScpAB
Spn Joint
parA
parA
parA
ΔparA

Figure S4

Figure S4. Construction and analysis of chimeric Smc proteins. Related to Figure 4.

A) Alignment of *Bsu* and *Spn* Smc amino acid sequences near the joint domain. Identical residues are highlighted by blue background colors. Splicing points between protein sequences are indicated in orange brackets. **B)** Viability of strains with Smc chimeras and wt *Bsu* ParB. **C)** Additional experiments for data shown in Figure 4A for different set of strains (from independently grown and analyzed samples). Several Smc chimeras shown in Figure 4A are probed, with Smc_{205} being included in the boxed insert (C*). **D)** Chromatin immunoprecipitation coupled to quantitative PCR (ChIP-qPCR) using α-ScpB serum undertaken on ^{Spn}joint strains containing ParB chimera proteins as indicated. Strains identical to those used for spotting in Figure 4B.

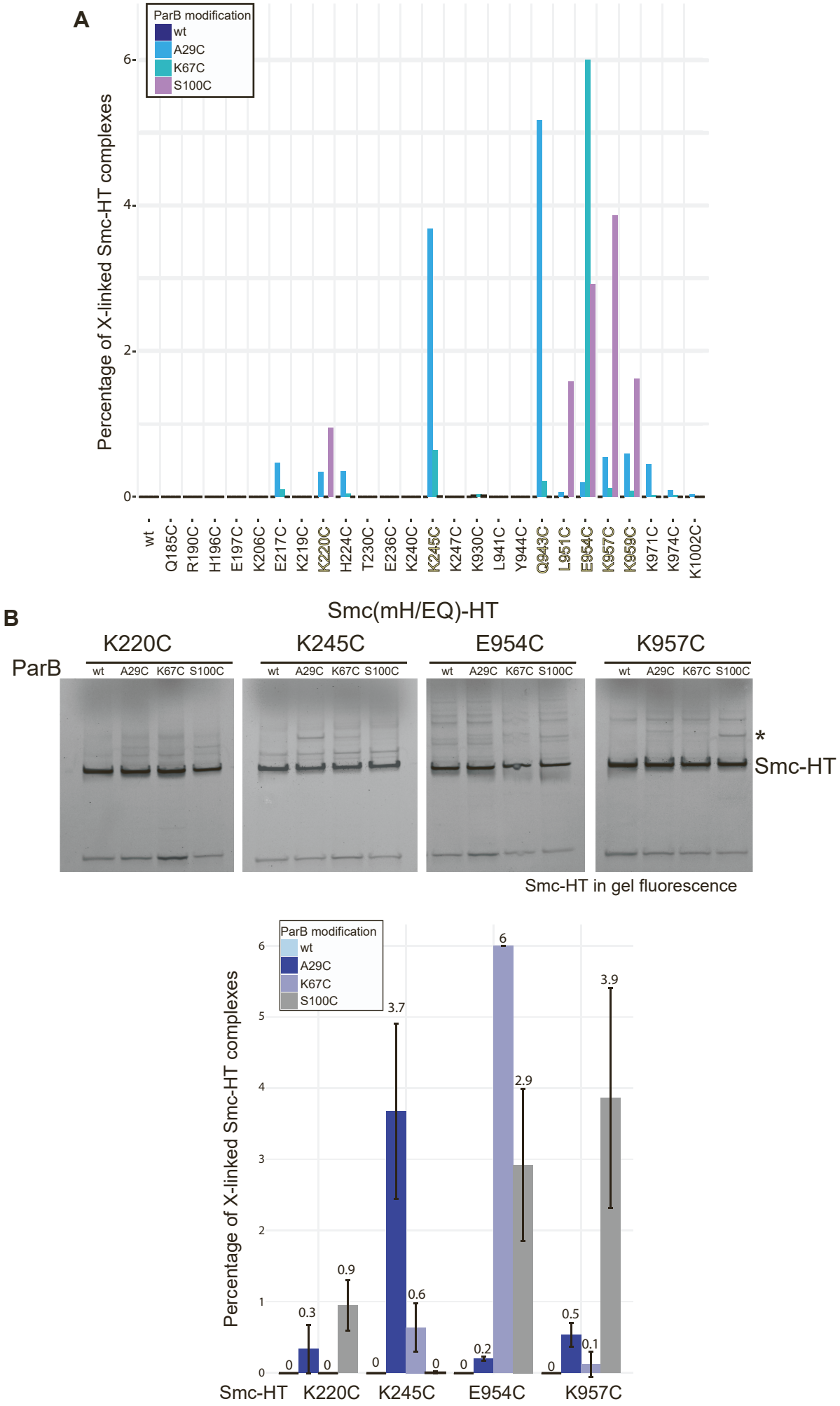
A
ParB modification
wt
A29C
K67C
S100C
Percentage of X-linked Smc-HT complexes
0
2
4
6
wt
Q185C
R190C
H196C
E197C
K206C
E217C
K219C
K220C
H224C
T230C
E236C
K240C
K245C
K247C
K930C
L941C
Y944C
Q943C
L951C
E954C
K957C
K959C
K971C
K974C
K1002C
B
Smc(mH/EQ)-HT
K220C
K245C
E954C
K957C
ParB
wt A29C K67C S100C
*
Smc-HT
Smc-HT in gel fluorescence
ParB modification
wt
A29C
K67C
S100C
Percentage of X-linked Smc-HT complexes
0
1
2
3
4
5
6
0
0.3
0
0.9
0
3.7
0.6
0
0
0.2
6
2.9
0
0.5
0.1
3.9
Smc-HT
K220C
K245C
E954C
K957C

Figure S5

Figure S5. Detection of Smc-ParB cross-linking. Related to Figure 5.

A) Screening combinations of ParB(Cys) and Smc(Cys) residues for BMOE cross-linking based on the detection of Smc(mH/EQ)-HT ('Smc-HT') protein by in-gel fluorescence. **B)** Cross-linking of selected Smc(Cys)-ParB(Cys) combinations as in Figure 5E but without pre-enrichment by ParB immunoprecipitation. Detection by in-gel fluorescence of Smc(mH/EQ)-HT protein. Representative gel images are shown (top panel). Quantification of BMOE cross-linking (bottom panel). Average values from three biological replicates are shown. Error bars denote standard deviation.

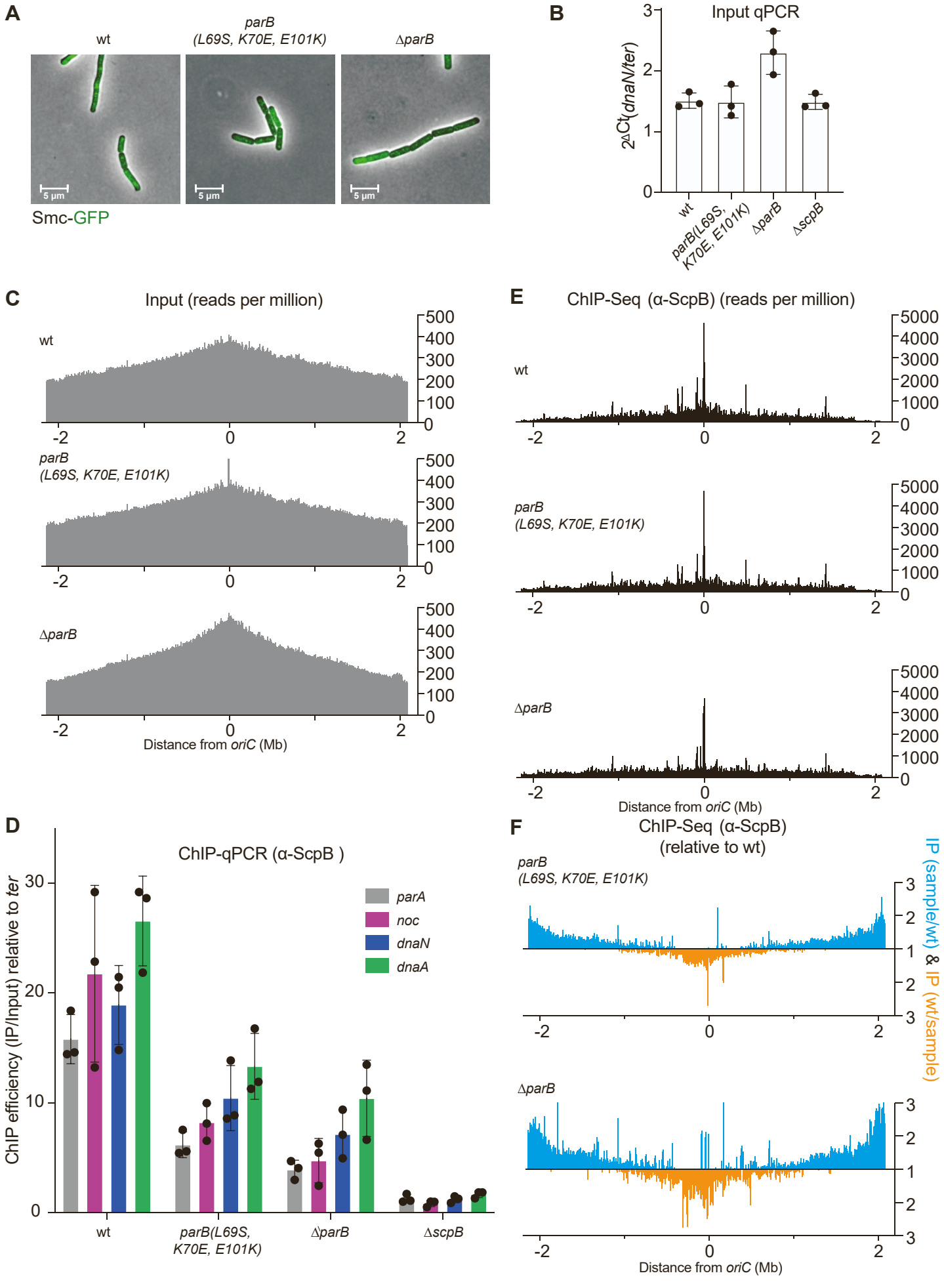
A
wt
parB
(L69S, K70E, E101K)
ΔparB
5 µm
Smc-GFP
B
Input qPCR
2^ΔCt(dnaN/ter)
wt
parB(L69S, K70E, E101K)
ΔparB
ΔscpB
C
Input (reads per million)
wt
parB
(L69S, K70E, E101K)
ΔparB
Distance from oriC (Mb)
E
ChIP-Seq (α-ScpB) (reads per million)
wt
parB
(L69S, K70E, E101K)
ΔparB
Distance from oriC (Mb)
D
ChIP-qPCR (α-ScpB)
ChIP efficiency (IP/Input) relative to ter
parA
noc
dnaN
dnaA
wt
parB(L69S, K70E, E101K)
ΔparB
ΔscpB
F
ChIP-Seq (α-ScpB)
(relative to wt)
parB
(L69S, K70E, E101K)
ΔparB
IP (sample/wt) & IP (wt/sample)
Distance from oriC (Mb)

Figure S6

Figure S6. Characterization of a joint-ParB interface mutant. Related to Figure 6.

A) Fluorescence microscopy of indicated *B. subtilis* strains with mGFP-tagged Smc. **B)** Relative enrichment of replication origin DNA (*dnaN*) compared to terminus-proximal DNA (*yocGH*) as judged by qPCR. For each strain, qPCR was performed on extracted genomic DNA (ChIP Input) using specific primers for *dnaN* and *yocGH*. $2^{\Delta Ct}$ values for the two loci were calculated to determine the relative enrichment of origin-proximal *dnaN* against *ter*. **C)** Deep-sequencing profiles of input DNA for the indicated strains. All deep-sequencing profiles were split into 1 kb bins with the origin of replication placed at position 0 Mb. Another representation of the data in shown in Figure 6G. **D)** Relative ChIP enrichment as measured by ChIP-qPCR performed with a polyclonal antiserum raised against the ScpB protein. ScpB enrichments at four tested origin-proximal loci *noc*, *parA* (*soj*), *dnaA* and *dnaN* were divided over that of terminus (*yocGH*) to obtain a ratio. Individual data points are shown as dots and error bars depict standard deviation from three biological repeats. **E)** ChIP-seq profiles of samples taken from D. All profiles were split into 1 kb bins with the origin of replication placed at position 0 Mb. Another representation of the data is shown in Figure 6H. **F)** Ratiometric analysis of *parB(L69S,K70E,E101K)* and Δ*parB* ChIP-seq (α-ScpB) profiles normalized to that of WT. For bins with read counts greater than the WT sample, the ratio was plotted above the genome coordinate axis (in blue). Otherwise, the inverse ratio was plotted below the axis (in orange). Another representation is shown in E and in Figure 6H.

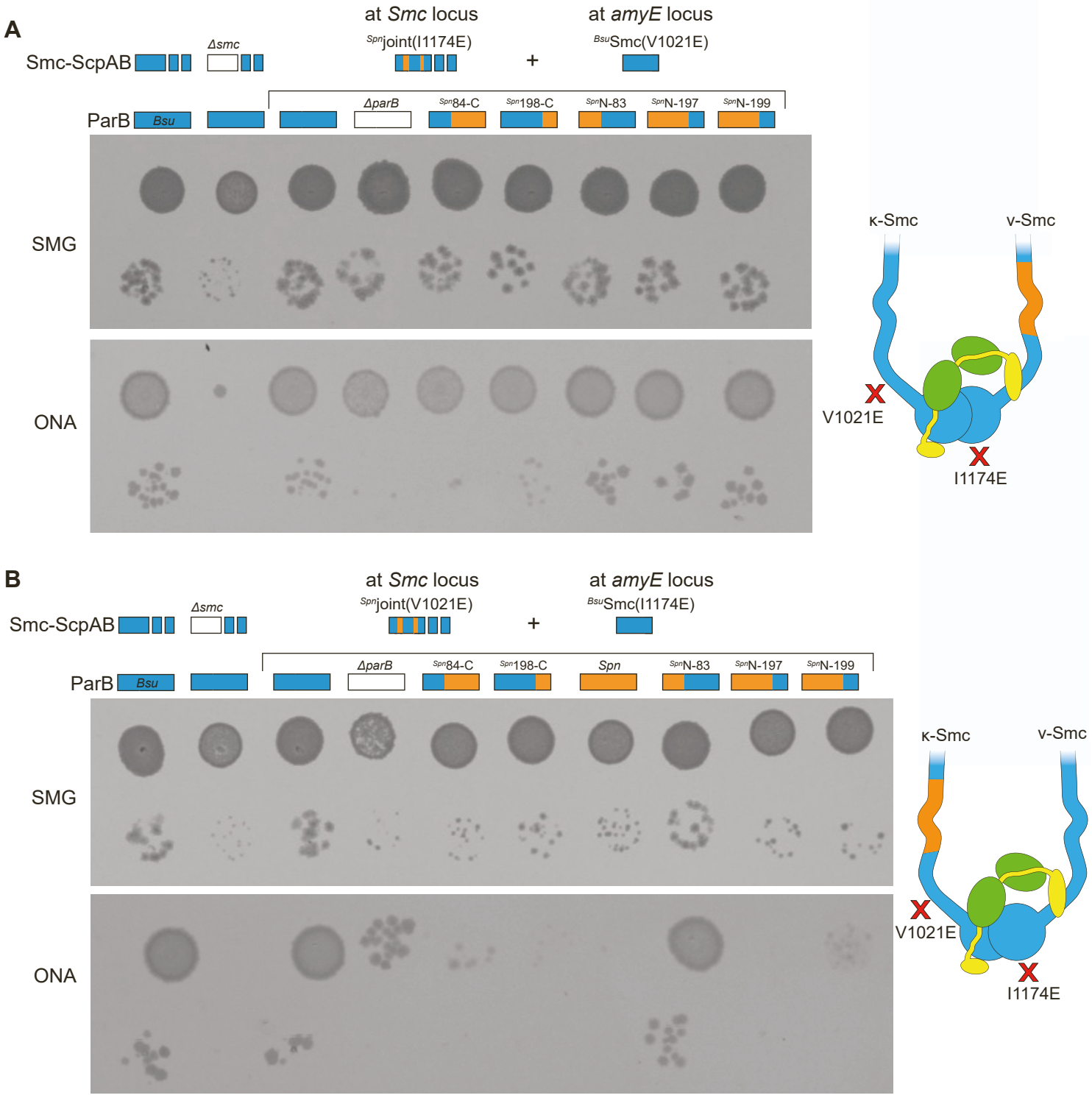
A
at Smc locus
at amyE locus
Δsmc
Spnjoint(I1174E)
+
BsuSmc(V1021E)
Smc-ScpAB
ParB
Bsu
ΔparB
Spn84-C
Spn198-C
SpnN-83
SpnN-197
SpnN-199
SMG
ONA
κ-Smc
ν-Smc
V1021E
I1174E
B
at Smc locus
at amyE locus
Δsmc
Spnjoint(V1021E)
+
BsuSmc(I1174E)
Smc-ScpAB
ParB
Bsu
ΔparB
Spn84-C
Spn198-C
Spn
SpnN-83
SpnN-197
SpnN-199
SMG
ONA
κ-Smc
ν-Smc
V1021E
I1174E
C
Smc
Smc
ParB MN dimer

Figure S7

Figure S7. Mapping of ParB residues involved in κ-Smc and η-Smc interactions. Related to Figure 7.

A) Spotting assay of strains carrying two different Smc alleles: a ^{Spn}Joint gene harboring the I1174E mutations expressed from the endogenous locus and an ectopic copy of the *Bsu* Smc gene carrying the V1021E mutation. The V1021E and I1174E point mutations block N-ScpA and C-ScpA binding, respectively. Only heterodimeric Smc dimers assemble functional Smc-ScpAB complexes. ParB chimeras as indicated. **B)** As in A but with V1021E and I1174E mutations swapped. **C)** Reconstruction of a ParB-Smc 2:2 complex using two Smc monomers (rod state) (in light and dark gray colors, respectively) and the ParB NM crystal structure (PDB: 6SDK) (in light and dark blue colors) using the predicted ParB-Smc structure as guide for superimposition.